이학박사 학위논문

Surface Study of Epitaxially Grown High Temperature Superconductor Thin Films using Scanning Tunneling Microscopy

주사형 터널링 현미경을 이용한 에피탁시 성장된 고온 초전도체 박막의 표면 연구

2018 년 8 월

서울대학교 대학원

물리천문학부

이선욱

Surface Study of Epitaxially Grown High Temperature Superconductor Thin Films using Scanning Tunneling Microscopy

주사형 터널링 현미경을 이용한 에피탁시 성장된
고온 초전도체 박막의 표면 연구

지도 교수 김 기 훈
이 논문을 이학박사 학위논문으로 제출함
2018 년 6 월

서울대학교 대학원
물리천문학부
이 선 욱

이선욱의 이학박사 학위논문을 인준함
2018 년 6 월

위 원 장 차 국 린 (인)
부위원장 김 기 훈 (인)
위 원 국 양 (인)
위 원 최 석 봉 (인)
위 원 서 정 필 (인)

Abstract

Surface Study of Epitaxially Grown High Temperature Superconductor Thin Films using Scanning Tunneling Microscopy

Sunwouk Yi

Department of Physics and Astronomy

The Graduate School

Seoul National University

Superconductivity has been the most actively studied field in solid physics since its discovery due to its unique natures perfect DC conductivity and perfect diamagnetism below the critical temperature. Though origin of superconductivity seemed to be solved at the microscopic level with help of the BCS theory, the emergence of cuprate high-temperature superconductors (HTS) and recently discovered Fe-based HTS require completely different explanations of the pairing mechanisms. In this study, epitaxially

grown HTS thin-films were studied using homebuilt low temperature scanning tunneling microscopy and spectroscopy (STM/STS) for understandings of high-temperature superconductivity. And the growth of high-temperature superconductors was performed using molecular beam epitaxy (MBE) or pulsed laser deposition (PLD), which has ability to transfer complex stoichiometry of target compound. For *in-situ* study of epitaxially grown samples, STM was used with Laser-MBE system. Details of the design and construction of the system are presented in this study. Co doped $BaFe_2As_2$ thin film, a member of "122" family of Fe-based HTS, was grown and studied using this system. $2\sqrt{2} \times 2\sqrt{2}$ R45° surface reconstruction which is different from that of the cleaved $BaFe_2As_2$, and the superconducting gap screened by the top barium layer were measured. And the charge modulation at the vicinity of the superconducting gap were observed. The thin film LiFeAs, belonging to "111" family, was grown by PLD technique for the first time. Optimization of growth and structural analysis of LiFeAs film are presented. The interrupted growth was used to improve the quality of the LiFeAs film and to grow close to the layer-by-layer manner.

Keywords: superconductor, iron-based superconductor, thin film superconductor, pulsed laser deposition, scanning tunneling microscopy

Student Number: 2011-23276

Contents

List of Figures

Chapter 1. Introduction

1.1 Overview

Superconductivity reveals a small gap near Fermi energy, but it has already enriched our lives in many areas of everyday life. For example, coils made of superconducting materials with no DC resistance can produce strong magnetic fields and are used in applications that require strong magnets, including nuclear magnetic resonance and magnetic resonance imaging. And superconducting quantum interference device magnetometer using Josephson phenomenon [1] allows precise magnetic field measurement. Not only that, there are various superconducting applications can be seen in industry and science, including particle acceleration, single photon detection, magnetic levitation systems, and lossless power transmission systems. However, superconducting phenomena only occur below the critical temperature. Thus, superconducting materials with higher critical temperatures can reduce the cost of cooling and lower the social costs of the aforementioned applications, which will make life more abundant. To do so, many scientists are looking for materials with higher critical temperatures.

Research to find superconducting materials with higher critical temperatures enriched our lives, but it is also important to study the mechanism of superconductivity in order to conquer superconductivity itself. Numerous studies for explaining the principles of superconductivity are being studied in various structures, systems and methods. In particular, a system of reduced dimensions, in which the dimension is less than characteristic length, is a good realm for studying physics. In the case of superconductors, the penetration depth and coherence length determine the dimensions of the system. A good example is a 2D superconducting system in which many topics such as quantum size effect, Berezinskii-Kosterlitz-Thouless transition [2] and quantum phase transition [3] are

actively studied. Crystallized thin film of 2D superconductor system have been available only through the development of deposition techniques such as molecular beam epitaxy (MBE) [4–8] and pulsed laser deposition (PLD) [9] and mechanical exfoliation [10] after recent 21st century. Before that, scientists could only do research in disordered systems, amorphous or granular thin films [11,12]. A critical temperature close to 80 K has been reported in 1ML of FeSe on $SrTiO_3$ system, which has a critical temperature of only 8 K in bulk [7]. Since then, research on 2D iron-based superconductivity has attracted much attention.

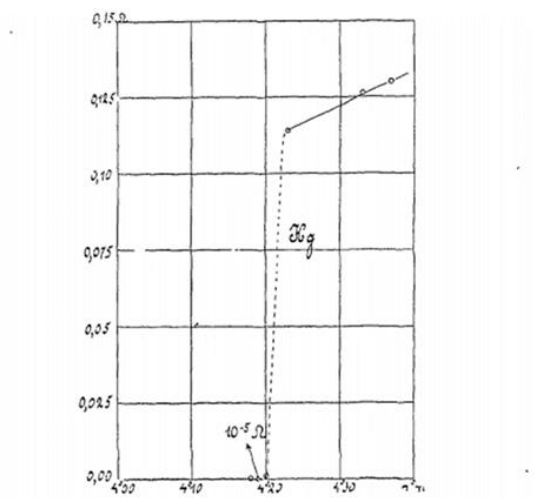

Figure 1.1: The Discovery of superconductivity: Resistance as function of the temperature plot of Hg in liquid helium bath. Image taken from [13].

In 1911, Superconductivity was first discovered by Heike Kamerlingh Onnes in Leiden laboratory [13]. In his work measuring the electrical resistance as function of the temperature, he found that the resistance of Hg dropped abruptly to zero at liquid helium temperature, and that an abrupt drop in resistance occurred in other materials. From a conventional point of view, if the temperature is lowered and the collision between the

electron and the electron or the lattice is reduced, the resistance may be lowered but not disappear even at zero temperature [14]. However, superconductors have zero resistance below the certain temperature, i.e., critical temperature T_c, which is the first hallmark phenomenon of superconductivity.

Another characteristic aspect of superconductivity is the Meissner effect [15]. It is not only excluding the magnetic field below the critical temperature, but also expelling out the magnetic field even when normal state transitions to superconducting state in the presence of a magnetic field. This phenomenon discovered by W. Meissner and R. Ochsenfeld in 1933 shows that superconducting materials are perfect diamagnetism. From the Meissner effect, superconductivity is destroyed not only by increasing the temperature, but also by the critical magnetic field $\overrightarrow{H_c}$. The difference in thermodynamic free energy between normal and superconducting states resulting from this critical field corresponds to superconducting condensation energy. Also, superconductivity is also destroyed by strong currents that satisfy the Silsbee criterion, i.e., $\overrightarrow{J_c}$.

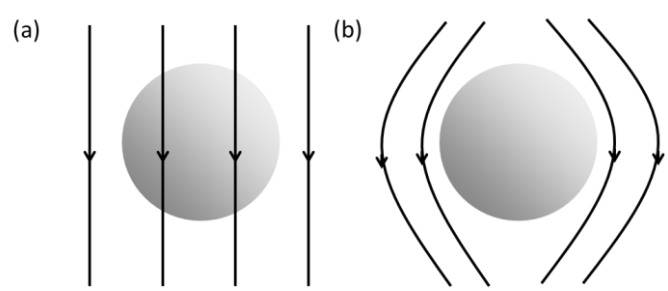

Figure 1.2: Schematic diagram of Meissner effect: A magnetic field line passing through a sample. In the normal state (a), the flux permeates the sample, but when it becomes the Meissner state (b), the magnetic flux is expelled.

In 1935 the London brothers proposed two equations to describe the electrodynamics of superconductors [16]. The two equations based on the Drude [14] model and the Maxwell equations are intended to explain the perfect conductor and the Meissner effect, respectively. The later equation which locally relating $\overrightarrow{J_s}$ with vector potential $\vec{A}$ gave the motif that superconductivity is based on quantum phenomena [17]. This local relation was later modified by Pippard to a non-local relation with dependence of characteristic length to explain better the penetration depth measurement [18,19].

There were phenomenal equations to describe superconductivity, but at the microscopic level there was no explanation of superconductivity until 1957. That year, J. Bardeen, L. N. Cooper, and J. R. Schrieffer proposed an idea that could microscopically describe superconductivity. This idea is the BCS theory [20]. The basic idea is that the Fermi sea with any bound pair resulting from an attractive interaction will become unstable and move to another lower ground state. This pair consists of two electrons whose momentum and spin are opposite to each other and have a coherence length scale. This pair is named Cooper pair after Cooper, who proved this. The origin of the attractive interaction was the lattice vibration claimed by Fröhlich, which was confirmed by the $M^{-1/2}$ dependence of T_c and H_c in isotope experiments [21]. The BCS theory can explain most of superconductivity phenomena in the weak coupling approximation limit. And the Eliashberg model [22], which does not drastically approximate the potential as in the BCS theory, can also explain the superconducting phenomenon of a material with a more complex phonon structure. The reason why this theory emerged only after 40 years of superconductivity was discovered was that the potential could not be solved by perturbation.

Even though there is BCS, there is a theory that was able to solve many questions from other directions. Ginzburg and Landau proposed a phenomenological theory using

complex order parameters seven years prior to the introduction of BCS theory [23]. This theory is based on Landau's general theory of second-order phase transition, where the order parameter corresponds to the local density of superconducting electrons.

And G-L theory describes type II superconductors which is classified by response to a magnetic field. This classification is defined by the ratio of the two characteristic lengths, $\kappa = \lambda/\xi$. If κ is less than $1/\sqrt{2}$, it is a type I superconductor, and if κ is greater than $1/\sqrt{2}$, it is a type II superconductor. Type II superconductors have two critical magnetic fields, H_{c1} and H_{c2}, and when the field is higher than H_{c1}, the Meissner state becomes a vortex state [24]. In the vortex state, the magnetic flux can penetrate superconducting in the form of a flux quanta, and the region becomes normal metal state called a vortex [25]. The vortex has a core size of ξ and circulating supercurrent around it. The field above H_{C2} makes the vortex state normal state. Note that if the order parameters are spatially uniform, the Ginzburg-Landau theory is equivalent to the London equations. Later, by Gor'kov, this theory appears to be derived by microscopic BCS theory and is considered to be more intrinsically approaching superconductivity, which is a macroscopic quantum mechanical state [26].

There have been notable advances in the theory of superconductivity, but there have been developments to increase the critical temperature and to find new types of superconductors. A relatively high transition temperature was found in the A-15 phase material [27], and studies were conducted under many compound and pressure conditions. In 1986, G. Bednorz and A. Muller discovered high-temperature superconductivity in the Ba-La-Cu-O system and opened a new horizon of high-temperature superconductors based on copper oxides [28]. The following year, YBCO recorded a critical temperature of 93 K [29], which is above the nitrogen temperature, and various copper based

superconductors were studied. In 2008, H. Hosono group found that high-temperature superconductors were found not only in cuprate series but also in iron-based superconductors [30,31]. Today, the highest critical temperature is 133 K of Hg based cuprate [32] and 203 K of H_2S under pressure [33], which is unimaginable only 20 years ago.

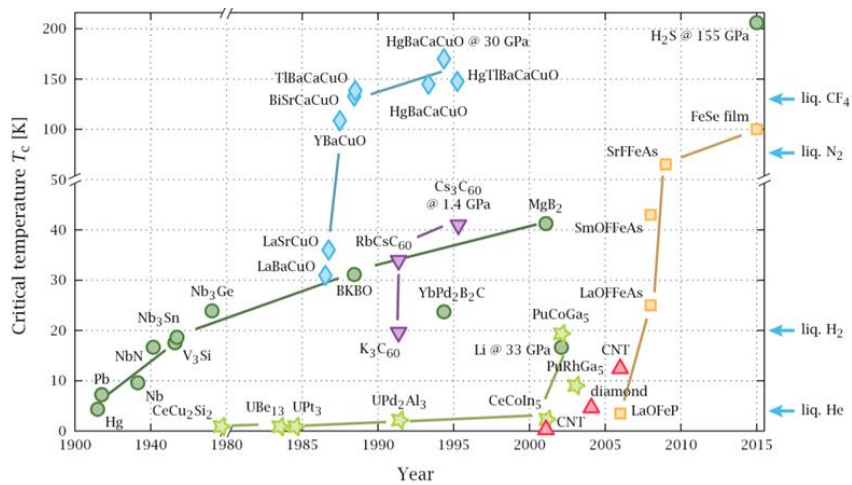

Figure 1.3: History of superconductors: Transition temperature of superconducting materials discovered over time. Different symbols are displayed depending on the type of superconductivity. Image taken from [34]

1.2 Conventional Superconductor

In the previous chapter, the characteristic phenomena of superconductivity were described and the historical milestones of superconductivity were reviewed. This chapter reviews the BCS theory of superconductivity for the first time at a microscopic level and discusses the microscopic description of phenomena in superconductivity. In terms of the

term, conventional superconductors refer to superconductors that can be explained by BCS theory, and unconventional superconductors do not. Most of the elemental superconductors belong to the conventional, while the niobium and vanadium are strangely elemental superconductors, but belong to type II.

In the BCS theory, the origin of the attractive interaction is the phonon, the lattice vibration [35]. The mechanism can be described as follows. When the electron moves in the lattice space, the lattice near the moving electron is distorted by Coulomb force leaving the region positively charged, and the other electrons passing through that region then feel the attractive Coulomb force. The following is a schematic diagram.

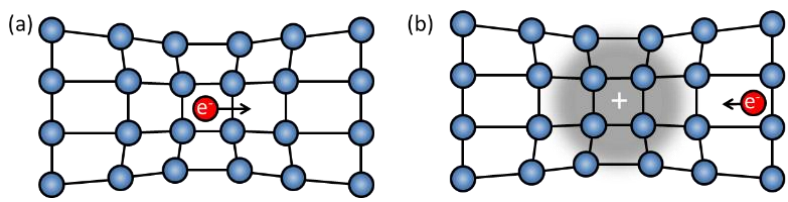

Figure 1.4: Simple schematic diagram of a pairing mediated by a phonon: (a) Electrons pass through lattice ions and distort by Coulomb force. (b) The area where the first electron left is positively charged for a moment, and the second electron feels the attraction.

The wave function of the Cooper pair is written as the product of the orbital and spin parts. Considering the total anti-symmetry of the wave function of the pair on exchange, the even parity orbital wave function has spin singlet state, that is, s-wave and d-wave, respectively, with an angular momentum quantum number l = 0, 2, ... Similarly, the odd parity orbital wave function has a spin triplet state. The BCS theory assumes an isotropic in real space, so it has s-wave orbital and spin singlet states.

The BCS theory is based on Cooper pair, which is mediated by lattice vibration. If at least one pair of electrons is bound to the attractive interaction, the Fermi sea becomes unstable regardless of the strength of attraction. The instability of the Fermi sea is maximized by the bound pairs with opposite momentum and spin, Cooper has shown that from the Fermi sea and Fermi statistics, and the pair is named Cooper pair after his name [36]. This instability can be seen using a simple model with two electrons added to the Fermi sea. The energy eigenvalues of the two electrons in this system are as follows [37].

$$E = 2E_F - \frac{2\hbar\omega_c e^{-2/N(0)V}}{1 - e^{-2/N(0)V}} \tag{1.1}$$

Where V is the interaction potential and N(0) is the density of state at the Fermi level. In this model, Cooper used a bold approximation, he set the potentials $V_{\vec{k}\vec{k'}}$ in the energy window from E_F to cutoff energy $\hbar\omega_c$ away from E_F isotropically to -V and set potentials to 0 in the other energy regions. In fact, if weak coupling approximation with N(0) V << 1 is possible, the binding energy is much smaller than $\hbar\omega_c$, and the momentum-dependent detail $V_{\vec{k}\vec{k'}}$ does not have much effect on the result.

Previously, it was confirmed that the Fermi sea had instability in the formation of the Cooper pair. The BCS wave function considering pair formation can be written using mean field approach by the idea of the J. Schrieffer rather than the N-electron slater determinant.

$$|\Psi_{BCS}\rangle = \prod_{\vec{k}} (|u_{\vec{k}}| + |v_{\vec{k}}| e^{i\theta} c^{\dagger}_{\vec{k}\uparrow} c^{\dagger}_{-\vec{k}\downarrow}) |\phi_0\rangle \tag{1.2}$$

Where, $|u_{\vec{k}}|^2 + |v_{\vec{k}}|^2 = 1$, and $u_{\vec{k}}$ and $v_{\vec{k}}$ represent the probability that electrons occupying and unoccupying the pair with state $\vec{k}\uparrow, -\vec{k}\downarrow$. And wave function $|\phi_0\rangle$ is the

Fermi sea occupied by electrons up to momentum $\overrightarrow{k_F}$. This many body wave function takes the form of a superposition of coherent cooper pairs. Cooper pairs are actually coherent macroscopic quantum states that are 10 to 100 nm in size and are spatially overlapping. And the Hamiltonian of this system is called pairing Hamiltonian or reduced Hamiltonian and has the following form.

$$H = \sum_{\vec{k}\sigma} \epsilon_{\vec{k}} n_{\vec{k}\sigma} + \sum_{\vec{k}\vec{l}} V_{\vec{k}\vec{l}} c^{\dagger}_{\vec{k}\uparrow} c^{\dagger}_{-\vec{k}\downarrow} c_{-l\downarrow} c_{l\uparrow} \tag{1.3}$$

In the BCS theory, the ground state is obtained by using the variational method, $u_{\vec{k}}$ and $v_{\vec{k}}$ are determined, and various physical quantities can be calculated. Further, by introducing the quasi Bose operator $b_{\vec{k}}$ and assuming that the fluctuation of $c_{-k\downarrow} c_{k\uparrow}$ is small, we can use the following model Hamiltonian.

$$H = \sum_{\vec{k}\sigma} \xi_{\vec{k}}\, c^{\dagger}_{\vec{k}\sigma} c_{\vec{k}\sigma} - \sum_{\vec{k}} (\Delta_{\vec{k}} c^{\dagger}_{\vec{k}\uparrow} c^{\dagger}_{-\vec{k}\downarrow} + \Delta^{\dagger}_{\vec{k}} c_{-\vec{k}\downarrow} c_{\vec{k}\uparrow} - \Delta_{\vec{k}} b^{\dagger}_{\vec{k}}) \tag{1.4}$$

And $\Delta_{\vec{k}}$ is defined as follows.

$$\Delta_{\vec{k}} = -\sum_{\vec{l}} V_{\vec{k}\vec{l}} b_{\vec{l}} = -\sum_{\vec{l}} V_{\vec{k}\vec{l}} \langle c_{-\vec{l}\downarrow} c_{\vec{l}\uparrow} \rangle \tag{1.5}$$

The Hamiltonian can be diagonalized by appropriate canonical transformations. N. N. Bogoliubov and J. G. Valatin introduced the following fermion quasi particle operator [38,39].

$$\begin{aligned} c_{\vec{k}\uparrow} &= u^{\dagger}_{\vec{k}} \gamma_{\vec{k}0} + v_{\vec{k}} \gamma^{\dagger}_{\vec{k}1} \\ c^{\dagger}_{-\vec{k}\downarrow} &= -v^{\dagger}_{\vec{k}} \gamma_{\vec{k}0} + u_{\vec{k}} \gamma^{\vec{\dagger}}_{\vec{k}1} \end{aligned} \tag{1.6}$$

After replacing the new operators defined above with the model Hamiltonian, $u_{\vec{k}}$ and $v_{\vec{k}}$, which make the coefficients of $\gamma_{\vec{k}1}\gamma_{\vec{k}0}$and $\gamma_{\vec{k}0}^{\dagger}\gamma_{\vec{k}1}^{\dagger}$ to zero, can be determined. At this time, the above model Hamiltonian becomes diagonalized.

$$H_M = \sum_{\vec{k}} (\xi_{\vec{k}} - E_{\vec{k}} + \Delta_{\vec{k}} b_{\vec{k}}^{\dagger}) + \sum_{\vec{k}} E_{\vec{k}} (\gamma_{\vec{k}0}^{\dagger}\gamma_{\vec{k}0} + \gamma_{\vec{k}1}^{\dagger}\gamma_{\vec{k}1}) \qquad (1.7)$$

The first term of Hamiltonian refers to the condensation energy, which is the energy difference between normal and superconducting state. The second term is described as a single particle excitation spectrum of quasi particles (Bogoliubons) created by $\gamma_{\vec{k}0}^{\dagger}$ and $\gamma_{\vec{k}1}^{\dagger}$.

$$E_{\vec{k}} = \sqrt{\xi_{\vec{k}} + |\Delta_{\vec{k}}|^2} \qquad (1.8)$$

The excitation spectrum of the quasi particle at this equation is $E_{\vec{k}}$. This Hamiltonian can be seen as behavior of a quasi-particle in a potential free system, using a wave function with the mean field approach and proper canonical transformation.

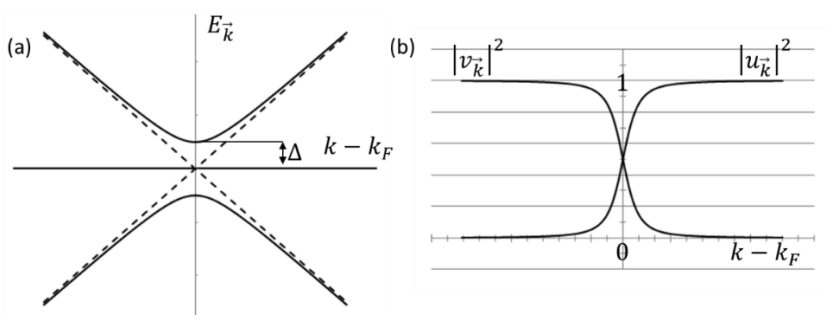

Figure 1.5: BCS energy spectrum and occupation: (a) Excitation spectrum of quasiparticle as function of k near the Fermi wave vector. The dashed line represents $\epsilon_{\vec{k}}$, the energy in the normal state. (b) Plot of BCS occupation parameter. $|u_{\vec{k}}|^2$, $|v_{\vec{k}}|^2$.

Furthermore, this approach can reveal several more properties. In the gap function, the coefficient obtained from the Variational method can be inserted to show the following temperature dependence.

$$\frac{1}{N(0)V} = \int_0^{\hbar\omega_c/2k_BT} \frac{\tanh x}{x} dx \tag{1.9}$$

And this integral gives the following results.

$$k_BT_c = 1.13\ \hbar\omega_c e^{-1/N(0)V_0} \tag{1.10}$$

By substituting the temperature zero for the gap function above, a simple expression can be obtained. And this equation shows the universal ratio of gap value and critical temperature of BCS superconductor.

$$\frac{2\Delta(0)}{k_BT_c} \approx 3.53 \tag{1.11}$$

1.3 Unconventional Superconductor

Conventional superconductors described by the BCS theory have an isotropic interaction potential due to phonon, and therefore energy gap Δ is not dependent on momentum. So the Cooper pair wave function also has an s-wave symmetric orbital with an orbital angular momentum $l = 0$. In 1986, IBM researchers Bednorz and Muller reported superconductivity with a transition temperature of 26 K in the $La_xBa_{1-x}CuO_4$ system [28]. Superconducting phenomena in copper oxides with transition temperatures above the boiling point of nitrogen have been reported in succession [29]. Magnetism had been known to be far from superconductivity, but interestingly parent compound of cuprate has

antiferromagnetism [40]. And the pairing potential is not symmetric with respect to $\vec{k}$, and the BCS theory cannot explain the critical temperature above 30 K [41]. Unconventional superconductivity, in which the superconducting mechanism is not explained by BCS theory, emerged.

Copper oxide-based superconductors appear in materials of insulating ceramic based perovskite crystals. These materials have an antiferromagnetic CuO_2 plane separated by a charge reservoir layer and superconductivity is controlled by electron or hole doping. The behavior of this Mott insulator has been studied extensively in the Hubbard model.

Unlike conventional superconductors, Cooper pair in the cuprate superconductors have d-wave pairing symmetry with an orbital angular momentum $l = 2$. The gap function has the following form.

$$\Delta(\theta) = \Delta_0 \cos 2\theta \tag{1.12}$$

The density of states of a full gapped s-wave superconductor has a U-shape gap, whereas a d-wave superconductor with $d_{x^2-y^2}$ order parameter has a V-shape gap. This is a spectroscopic feature of unconventional superconductors with gap node due to anisotropic potential. In addition to this spectroscopic feature, cuprate is distinguished from conventional superconductors in relatively large energy gap ~ 50 meV and pseudogap phase.

In 2008, when H. Hosono group discovered superconductivity in LaFeOAs materials, unconventional superconductors were again spotlighted [30]. Fe has magnetic properties, and the parent material also has a magnetic order, so Fe-based superconductors are thought far from BCS. Nonetheless, numerous reports of iron-based superconducting materials have opened the so-called iron-age of superconductors [7,30,42,43]. Iron and pnictogen

or chalcogen compound layers in Fe-based superconductors resemble copper oxygen plaquette in cuprates, and these materials are also controlled by superconducting by electron or hole doping [44]. The most widely considered gap structure is s ++ or s +-, defined by the sign change of the gap function between the hole pocket and the electronic pocket [45]. Structural phase, electronic structure, or AFM fluctuation properties are studied, but it is difficult to say that it is a universal feature.

In addition, there are unconventional superconductors such as heavy fermions and organic salts, but due to their low Tc and their importance in research, unconventional superconductors usually refer to copper oxide or iron-based superconductor.

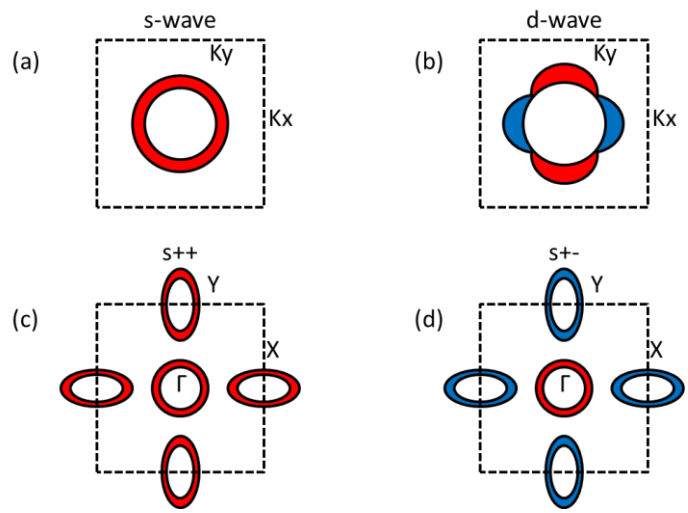

Figure 1.6:Schematic illustration of Fermi surface and structure of gap function Δ_k: Red means gap sign is positive, blue means negative gap sign.

1.4 Thin Film Superconductor

According to the Mermin Wagner theorem [46], the lower the dimension, the more likely the phase coherence of the long range is disturbed by the thermal fluctuation. Therefore, it has been known for a long time that cooper pair formation is difficult in 2D. And under a reduced dimensionality it is more difficult to have a long range order due to inevitable defects. Therefore, thin film superconductivity was difficult to study until a technique for depositing a clean and crystalline film was developed.

Early thin-film superconductivity studies were limited to the study of amorphous or granular films made with quench-condensed methods [11,12]. Studies at this time focused on the degree of disorder and scaling behavior of the film. Over the last several decades, material deposition techniques have evolved a lot and techniques such as MBE, PLD, thermal evaporation, and sputtering have developed remarkably. In addition, the measurement technique has also developed rapidly, enabling direct access to highly crystalline atomic thickness films by *in situ* UHV low temperature measurement or scanning tunneling microscopy / spectroscopy. With the help of these technologies, the following researches are currently underway. The monolayer superconductivity study of elemental metal thin films on silicon and the oscillation of critical temperature depending on the thickness due to the quantum size effect [4,47]. A study of electrically tuning 1 UC of cuprate high-temperature superconductor, $La_{2-x}Sr_xCuO_4$, from superconductor to insulator [6]. A study on the superconductivity of 2 DEG at the interface between $LaAlO_3$ and $SrTiO_3$ [48]. And one of the most surprising recent studies is the epitaxially grown 1 UC FeSe on $SrTiO_3$(100) system [7]. FeSe has a critical temperature of only 8 K in bulk, but with 1 UC thickness, the critical temperature increases to ~ 100 K. The research on 2D superconductivity triggered by this research is once again in the revival period.

1.5 Scope of the Thesis

The goal of this thesis is to study the surface and electronic structure and optimize the growth of iron-based superconducting thin films. The studied materials are Co doped $BaFe_2As_2$ and LiFeAs. In order to achieve the goal, we built a system that combines Laser-MBE and scanning tunneling microscopy. The system consists of a chamber for growing the sample, a scanner chamber for measuring the grown sample, and a preparation chamber for preparing the sample. The Laser-MBE chamber is designed to grow the sample. The Laser-MBE chamber is designed to characterize growth details using reflection high energy electron diffraction and low energy electron diffraction techniques. The grown samples from this chamber can be transferred to the scanner chamber without breaking UHV. Our approach is to analyze diffracted electron structure for growth parameters when the sample is grown and to measure the surface morphology and electronic structure in real space using STM. The following is the scope of this paper.

Chapter 1 describes the background theory of superconductivity and briefly explains issues on superconductivity research.

Chapter 2 briefly describes the film growth mode, model and kinetics. The basic concepts and operation principle of MBE and PLD. the epitaxial film growth techniques used in this study, are presented. And details of RHEED, LEED and STM surface analysis apparatus used in this research are described.

Chapter 3 introduces the design and construction of Laser-MBE systems. This chapter contains considerations when designing the system, details of setup and system performance is presented.

Chapter 4 discusses Co-doped $BaFe_2As_2$, an iron-based superconductor material. Growth details and STM measurements of $Ba(Fe_{1-x}Co_x)_2As_2$ thin films grown using the system described in the previous section are discussed. The optimization of growth and the unique surface structures that occur in the PLD process are described. We will also study superconductivity by analyzing the electronic structure obtained using STS and transport measurement.

Chapter 5 deals with another iron-based superconductor material, LiFeAs, which belongs to the 111 family. As in the previous chapter, the growth and STM measurement of LiFeAs thin films are discussed. And the growth details and optimization of growth is discussed.

Chapter 2. Film Growth and Surface Analysis

This section briefly describes the film growth mode, models and kinetics. The basic concepts and operation principle of MBE and PLD, the epitaxial film growth techniques used in this study, are presented. And Details of RHEED and LEED surface analysis apparatus used in this research are described.

2.1 Film Growth

In growing epitaxial thin film, the atomically smooth film surface and sharp interface have a significant role in the desired character and high quality application performance of the film. Therefore, it is important to study the ability to control surface morphology in stacking thin film layers and also to understand the growth mechanism to create the desired structure. These studies have helped us to approach the artificially fabricated structures with atomic precision. In addition, researches on revealing thin film growth mechanism has been carried out as a research field itself as well as helping to grow good samples.

Technically, over the past decade, thin film deposition techniques have made many advances. In particular, the method of growing high temperature superconductors (HTS) and related oxides related to this study has been successful [49–51]. During this period, various HTS phases, artificial HTS compounds, precise multilayer and supper-lattice structures were realized with high quality. MBE [7,52,53] and PLD [9,49] are typical examples of a method of depositing a good quality thin film. Depending on the purpose, thermal evaporation, sputtering, and chemical vapor deposition are used in the proper place. These physical vapor depositions include two fundamental processes: Nucleation, which is the formation of the cluster, and growth, which is the lateral expansion of the step. Here,

the author will summarize the growth mode and growth kinetics during deposition and the elementary models describing early stage of growth.

2.1.1 Growth Modes

Before discussing epitaxial film growth, the term epitaxy is described as follows. Epi means above in Greek and taxis means ordered manner. That is, it is translated into "arranging upon". Naturally, epitaxy growth refers to a technique of depositing a crystalline over-layer on a crystalline substrate. Homoepitaxy is the method of growing the crystalized layer on the same material substrate, and heteroepitaxy is the technique for growing crystalline film on crystalline substrate of a different materials. This method is often used to create structures that do not exist in the natural world if not artificially created The substrate and epitaxial layers involved in heteroepitaxy are lattice mismatched materials facing each other and the relative lattice misfit is defined as follows.

$$f = \frac{(a_e - a_s)}{a_s} \tag{2.1}$$

Where a_e and a_s are the bulk lattice constants of the epitaxial layer and substrate, respectively. The lattice constants of alloys in which some are substituted with other materials follow Vegard's law [54].

The next part to discuss is what film morphology the epitaxial layer grows with. If the grown thin film and substrate systems are close to thermal equilibrium, i.e., supersaturation is small or moderate, a thermodynamic approach can be used to determine the growth mode. In this approach, the growth mode is determined by the balance of the surface energy of the island γ_i, the surface energy of the substrate γ_s, and interface energy between the

island and the substrate γ_{i-s}. The three modes described in the figure represent a typical film growth mode in which the balance of surface energy is determined [55].

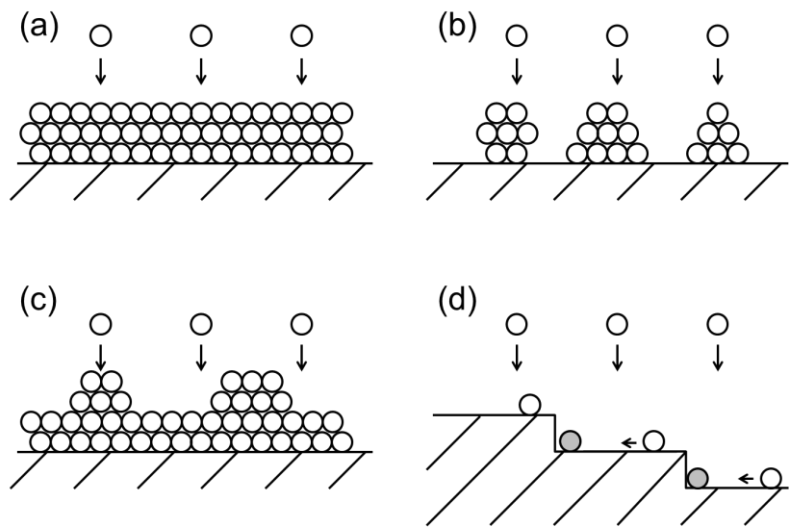

Figure 2.1: Illustration of typical growth mode: (a) Frank-Van der Merwe (Layer-by-layer) mode, (b) Volmer-Weber mode (island), (c) Stranski-Krastanov (Wetting+island), (d) Step flow growth mode.

In the layer by layer mode (Frank-van der Merwe mode), the adatom tends to attach more to the substrate surface with less lattice mismatch system. In this growth mode, the interfacial energy γ_{i-s} is small due to the strong bonding between the film and the substrate. And the surface energy of the substrate is larger than the sum of the rest ($\gamma_s > \gamma_{i-s} + \gamma_i$). On the other hand, if γ_s is smaller than the sum of the remaining γ_{i-s} and γ_i, the 3D island is nucleated on the surface. In this 3D growth mode (Volmer-Weber mode), the adatoms are adhered to each other when the overlayer has a large lattice misfit or the bonding force between the thin film and the substrate is weak. This film has a nature that does not wet the substrate in order to minimize the total energy. The next mode to be

described is the Stranski-Krastinov mode, which is a growth mode that occurs mainly in the heteroepitaxial growth. In this mode, the thin film grows up to the critical thickness by the layer by layer method, and then transitions to 3D island growth. The critical thickness is usually a few monolayer. In heteroepitaxy growth with moderate lattice mismatch (2~10%), the biaxial strain between the substrate and the film becomes stronger as the thickness increases. As the thickness increases, the stronger strain creates a misfit dislocation, and the resulting increase in energy becomes larger than the increase in interface energy due to dislocations, so making the 3D islands is energetically favorable. It is the core of S-K mode to make equilibrium defect by strain relaxation.

2.1.2 Growth Kinetics

In determining the growth mode, a thermodynamic approach can be carried out in thermodynamic equilibrium, discussed earlier. However, the kinetic approach to determining surface morphology must be considered at the same time. This is because nucleation and growth of a cluster are kinetic effects far from thermal equilibrium. Especially for homoepitaxial growth, surface diffusion coefficient plays more crucial role in determining surface morphology than surface energy consideration. Consider the case where the adatom migrates on the surface. The distance of diffusion before the adatom re-evaporates can be written as follows [56].

$$l_D = \sqrt{D_s \tau} \tag{2.2}$$

Where τ is the time staying on the surface before re-evaporation. And the diffusion coefficient D_s can be expressed as follows [57].

$$D_s = va^2 exp(-\frac{E_A}{k_B T}) \quad (2.3)$$

The coefficients are as follows. E_A is the diffusion activation energy, v is the attempt frequency and a is the characteristic jumping distance. Considering kinetics, surface diffusion can be divided into intralayer mass transport, which is the movement of the adatom on the terrace, and interlayer mass transport, which is the hopping to the lower layer. If intralayer mass transport is large enough so that l_D is larger than the average terrace size, step flow growth will occur in this case. The adatom sticks and nucleates on the terrace edge after the diffusion on the terrace. Therefore, step flow growth occurs well at high temperatures with long diffusion, low flux, and high step density on the vicinal surfaces. If intralayer mass transport is not sufficient, nuclei formation occurs on the terrace. The morphology of this growth mode is determined by interlayer mass transport.

2.1.3 Growth Models

The epitaxial thin film growth using the physical vapor deposition technique consists of nucleation and cluster growth. Then, the film is formed as a coalescence phenomenon of this cluster. These surface morphologies were discussed previously in case of thermodynamic equilibrium and considering kinetics. We will continue to discuss the model and basic concept of the initial stage of growth far from thermodynamic equilibrium.

Capillarity Theory

Various atomic processes take place on the substrate during thin film deposition. cluster nucleation, re-evaporation from substrate / cluster, deposition on substrate / cluster, and diffusion to / of cluster. This process is illustrated in the following figure [57].

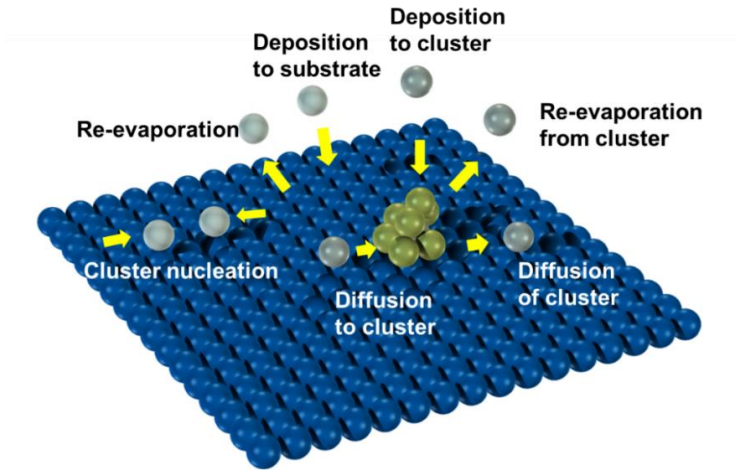

Figure 2.2: Atomic process during film deposition

These atomic processes involve a change in free energy. And the change of free energy is expressed as follows when a droplet of radius r is condensed

$$\Delta G = a_1 r^2 \sigma_{fg} + a_2 r^2 \sigma_{fs} - a_2 r^2 \sigma_{sg} + a_3 r^3 \Delta G_v \tag{2.4}$$

Where σ_{ab} are the surface tension. g, f, and s denote gas, film, and substrate, respectively. And ΔG_v is the specific sublimation energy, the term associated with supersaturation. Supersaturation is defined as the ratio of the gas phase condensation rate on the substrate and re-evaporation rate into the gas phase. The supersaturation S is given by

$$S = \frac{R_C}{R_r} = \frac{P}{P_D} \frac{\sqrt{T_S}}{\sqrt{T}} \tag{2.5}$$

R_C is the condensation rate and R_r is the re-evaporation rate. P is the gas pressure and P_D is the vapor equilibrium pressure of the film. And condensation rate and re-evaporate rate is given by

$$R = \frac{P}{\sqrt{2\pi M k_B T}} \tag{2.6}$$

In the case of condensation rate, T is the temperature of the adatom and in the case of re-evaporation, P is P_D and T is the temperature of the substrate. ΔG_v is expressed with respect to S defined above. And V_0 is the volume of the atom.

$$\Delta G_v = -\frac{k_B T}{V_0} \ln S \tag{2.7}$$

The free energy minimizes the energy at the critical radius, which can be obtained from the derivative of the radius of free energy. Hence

$$r_c = \frac{2(a_1\sigma_{gf} + a_2\sigma_{fs} - a_2\sigma_{sg})}{3a_3\Delta G_v} = \frac{2V_0(a_1\sigma_{gf} + a_2\sigma_{fs} - a_2\sigma_{sg})}{3k_B T a_3 \ln S} \tag{2.8}$$

The following is found through the temperature dependence of the critical size of the cluster ($\partial r_c/\partial T > 0$). Small clusters are created at low temperatures. The cluster size increases at high temperatures. That is, it shows a tendency to have a single crystal at a high temperature. And, considering the dependence of the critical dimension on the condensation rate (≈deposition rate), it can be seen that the lower the deposition rate, the larger the cluster size ($\partial r_c/\partial R < 0$).

Kinetic Models

This is a kinetic model that describes the change in cluster density as function of time. When the 2D growth occurs, the dimer is stable when it does not move. When there is isotropic diffusion without re-evaporation, the situation is described as follows [58].

$$\frac{dn_1}{dt} = F - 2\sigma_1 D n_1^2 - \sigma_x D n_1 n_x - F(Ft - n_1) - F n_1$$
$$\frac{dn_x}{dt} = \sigma_1 D n_1^2 + F n_1 \quad (2.9)$$

The above equation is for n_x, which is a stable island density with size x. The monomer density increases with increasing flux but decreases with diffusion and direct impinging. On the other hand, the density of stable island is increased by dimer formation of monomer and direct impinging. Furthermore, the island density can be obtained as a function of flux and diffusion coefficient through computational methods [59].

Zone Models

A model describing the morphology of thin films as a function of substrate temperature and incident energy (oxygen pressure in the case of oxide growth) [60]. It describes how the surface morphology appears in each zone divided into four zones depending on the incidence energy and substrate temperature. It is based on the nuclei formed by diffusion on the surface until it reaches the critical size. If the diffusivity is large enough, the island merges to form a smooth, continuous film.

2.2 Molecular Beam Epitaxy

Theoretical background and models for the physical phenomena during thin film deposition by physical vapor deposition technique have been discussed previously. In this section, operating principles and basic concepts of the MBE which is one of the deposition techniques used in this study. MBE is a technique for depositing high quality epitaxial thin films by reactant released from the source reaching the substrate and forming a crystalline

thin film. It is the first technique studied by Alfred Cho of Bell Telephone Labs in the late 1960s [61]. Although Davey and Pankey first performed the technique in 1968 [62], the term molecular beam epitaxy became known by Cho in 1970.

As compared to other PVD techniques, the prominent side of the MBE is usually at a deposition rate of less than $1\,\mathrm{nm/s}$. At this rate, the growth temperature window is large and epitaxial growth occurs. At rate less than $10^{10}\mathrm{cm^{-2}s^{-1}}$, island growth occurs and at more than $10^{20}\mathrm{cm^{-2}s^{-1}}$, amorphous growth occurs. The UHV condition is essential for this rate of deposition to be possible. So, another characteristic is that it is carried out in UHV. The MBE has detailed features due to its performance in UHV. First, the atomic or molecule reactants going out from the source go straight to the substrate.

$$\lambda_{mfp} = \frac{k_B T}{\pi d^2 P} \tag{2.10}$$

The above equation is the mean free path of the particles, where d is the collision diameter and P is the pressure. In UHV (~10^{-10} Torr), the long mean free path (~10^6 m) makes what is called a molecular beam. This straightness reduces unwanted interactions during flight and allows for high quality growth. Second, UHV environment lowers the impurities level during the crystallization process of the film. Finally, it enables in situ characterization such as RHEED. Since RHEED to be described later can measure thickness variations, it also has the advantage of enabling precise thin film growth control at the atomic level through the evaporator shutter control [56,63].

MBE has also an advantage in that each material evaporates independently from its effusion cell, requiring only the ingredients of the material to grow. it means that no precursor is needed such as other technique. it is an extremely flexible technique in which multiple sources can be used and various parameters are performed independently.

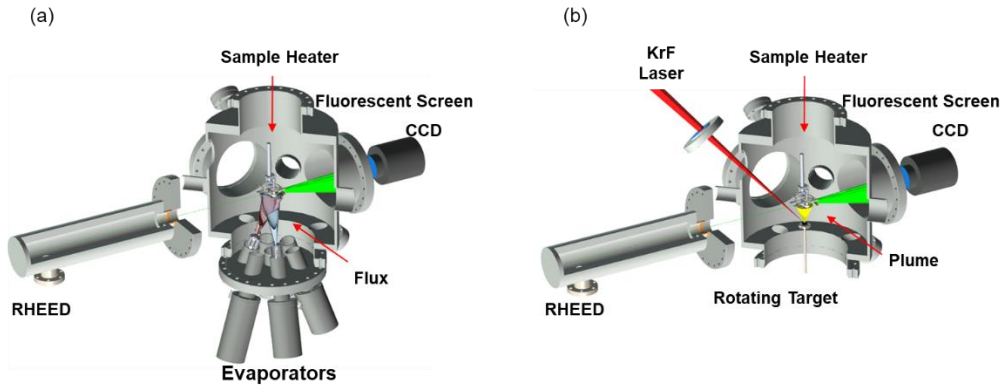

Figure 2.3: Comparison of schematic views: (a) MBE and (b) PLD

2.3 Pulsed Laser Deposition

In this study, thin film deposition was performed by PLD along with MBE. PLD technique, in which a high energy pulsed laser beam hits a target and causes the material to deposit, is one of the physical vapor deposition techniques. In 1960, T. H. Maiman first made laser [64], and in 1965 H. Smith and A. Turner deposited thin films with ruby laser [65]. It was not that the laser function was excellent, and it did not make very good quality film deposition compared to other techniques, but this is the birth of PLD. Since then, many improvements have been made to laser such as increased repetition rate, Q switching technique, and stability. A laser fluence over threshold ablation that can transfer the stoichiometry of the target is possible by strong and short pulses. Thus, in 1987, the HTS material, Y123, was grown by PLD technique [49]. Research has been initiated to develop functional thin oxide films including high-temperature superconductors which has been known to be difficult to deposit.

The operating principle of PLD is as follows. A high energy laser pulse is focused and strikes the target. When the laser pulse is absorbed into the surface layer of the target, a strong electric field is generated and electronically excited in the region. This electron excitation transfers their energy for a few picoseconds via lattice vibration by electron phonon coupling. In the beginning of pulse, this transferred energy creates a dense layer on the surface of the target and during the pulse the laser which so-called the Knudsen layer makes the layer heated, accelerated and expanded. This expanded layer, containing ions with kinetic energy of a few hundreds of eV [66] and neutrals of the kinetic energy of a few eV [67], is called a "plasma plume". Their kinetic energy is much larger than that of thermally evaporated atoms (~0.1 eV). This kinetic energy difference contributes to the different surface morphology of the thin films of MBE and PLD. The plume generated from the target material are directed in a normal direction from the target surface, and the distribution has a $cos^n\theta$ where n is from 4 to 30. And this depends on the background gas, and there are various models to explain it, such as drag force model and shock wave model.

In the case of ceramic materials, the threshold for ablation is lower than metal. This is because the thermal diffusion length is shorter than the optical absorption depth. In the case of metal, the optical absorption depth is shorter than the thermal diffusion length. Therefore, the pulse energy is dispersed to the diffusion length, it is hard to ablate. Among metals, refractory metal is difficult to ablate (~10 J/cm^2), and transition metal is ablated at (1~2 J/cm^2) [59].

PLD is characterized by transferring the stoichiometry of the target. Therefore, PLD has a strength in the growth of materials with complicated compositional material such as ternary and quaternary which is difficult to achieve with MBE. Another feature is the high

deposition rate. The high instantaneous deposition rate and the interval between the pulses is the feature of PLD. Therefore, it has a very high supersaturation *S* higher than 10^{13} and a small critical cluster radius r_c. These small clusters create a higher nucleation density. Thus, PLD grown films show surface morphology with higher island density than MBE films with the same average deposition amount. Clusters smaller than the critical radius during the pulse interval may merge or grow and exhibit unique morphology such as Ostwald ripening.

In the thin film deposition through PLD, droplets or fragments may be generated on the surface. Its size also reaches a few μm. It is a native problem, which can be minimized by ablation that is slightly above the threshold. And non-uniformity of the sample due to the narrow angular dependence of the plume can be a problem. This problem can be reduced by off axis geometry, shadow mask and by rotating the sample or target.

2.4 Reflection High Energy Electron Diffraction

Basic Electron Diffraction

Before dealing with surface analysis tools using electron diffraction, a brief description of the scattering and diffraction theory of electrons will be addressed [68]. Let the unit vector span the 3-dimensional lattice space $\overrightarrow{a_1}$, $\overrightarrow{a_2}$ and $\overrightarrow{a_3}$. In this study, we are interested in the 2D thin film. The waves scattered by the two-dimensional system are as follows.

$$\Psi = A_0 exp(i\overrightarrow{k'} \cdot \vec{r} - \omega t) \sum_l f_l exp(-i\vec{q} \cdot \overrightarrow{R_l}) \tag{2.11}$$

Where A_0 is the wave amplitude, f_l is the scattering factor of l-th scatter and $\overrightarrow{R_l}$ is the position of the atom of the *l*-th lattice and can be expressed as $\overrightarrow{R_l} = n_1\overrightarrow{a_1} + n_2\overrightarrow{a_2} + \overrightarrow{r_l}$. And $\overrightarrow{r_l}$ is the relative distance in the *l*-th unit cell. Also $\overrightarrow{k'} = \vec{k} + \vec{q}$ where $\vec{q}$ is momentum transfer. *l* summation runs over all atoms in the lattice sites. Dropping the amplitude and plane wave term that do not affect the intensity of the scattered beam, so the equation is rewritten as:

$$\begin{aligned}
\Psi &= \sum_l f_l \, exp\left(-i\vec{q}\cdot\overrightarrow{R_l}\right) \\
&= \sum_n f_n \, exp(-i\vec{q}\cdot\overrightarrow{r_n}) \left[\sum_{n_1=1}^{N_1} \exp(-i\vec{q}\cdot n_1\overrightarrow{a_1}) \sum_{n_2=1}^{N_2} \exp(-i\vec{q}\cdot n_2\overrightarrow{a_2})\right] \\
&= \sum_n f_n \, exp(-i\vec{q}\cdot\overrightarrow{r_n}) \left|\frac{exp(-iN_1\vec{q}\cdot\overrightarrow{a_1})}{exp(-i\vec{q}\cdot\overrightarrow{a_1})} \frac{sin(\frac{1}{2}N_1\vec{q}\cdot\overrightarrow{a_1})}{sin(\frac{1}{2}N_1\vec{q}\cdot\overrightarrow{a_1})}\right| \\
&\qquad \times \left|\frac{exp(-iN_2\vec{q}\cdot\overrightarrow{a_2})}{exp(-i\vec{q}\cdot\overrightarrow{a_2})} \frac{sin(\frac{1}{2}N_2\vec{q}\cdot\overrightarrow{a_2})}{sin(\frac{1}{2}N_2\vec{q}\cdot\overrightarrow{a_2})}\right|
\end{aligned} \tag{2.12}$$

The above calculations were carried out on a lattice space with N_1 and N_2 unit cells in the $\overrightarrow{a_1}$ and $\overrightarrow{a_1}$ directions, respectively. And the n-summation of the first term go over the basis of the unit cell. Therefore, the intensity of the scattered wave is as follows.

$$I = |\Psi|^2 = \left|\sum_n f_n \, exp(-i\vec{q}\cdot\overrightarrow{r_n})\right|^2 \left|\frac{sin(\frac{1}{2}N_1\vec{q}\cdot\overrightarrow{a_1})}{sin(\frac{1}{2}\vec{q}\cdot\overrightarrow{a_1})}\right|^2 \left|\frac{sin(\frac{1}{2}N_2\vec{q}\cdot\overrightarrow{a_2})}{sin(\frac{1}{2}\vec{q}\cdot\overrightarrow{a_2})}\right|^2 \tag{2.13}$$

In this equation, the first term is the structure factor due to atoms inside the unit cell consisting of n basis, and the remaining term is from the long range contribution. And if

the system have large N_i $(i = 1,2) \gg 1$, then the $\left|sin(\frac{1}{2}N_i\vec{q}\cdot\overrightarrow{a_i})/sin(\frac{1}{2}\vec{q}\cdot\overrightarrow{a_i})\right|^2$ term has a shape similar to a series of delta functions with peaks when $\frac{1}{2}\vec{q}\cdot\overrightarrow{a_i}$ is an integer multiple of π. Therefore, the scattered beam has the highest intensity when the following condition is satisfied.

$$\vec{q}\cdot\overrightarrow{a_1} = 2h\pi, \qquad \vec{q}\cdot\overrightarrow{a_2} = 2k\pi \tag{2.14}$$

Where *h*, *k* is integer. This scattering condition is Laue condition. In the momentum space, the peak has a separation corresponding to 2π times the reciprocal of the unit vector length in each direction. As a generalization, the unit vector in the momentum space for scattering is as follows.

$$\overrightarrow{b_1} = \frac{2\pi\overrightarrow{a_2}\times\hat{n}}{\overrightarrow{a_1}\cdot\overrightarrow{a_2}\times n}, \qquad \overrightarrow{b_2} = \frac{2\pi\overrightarrow{a_1}\times\hat{n}}{\overrightarrow{a_1}\cdot\overrightarrow{a_2}\times n} \tag{2.15}$$

And this equation satisfies the following relation.

$$\overrightarrow{a_i}\cdot\overrightarrow{b_j} = \delta_{ij} \quad (i,j = 1,2) \tag{2.16}$$

The space spanned by $\overrightarrow{b_1}$ and $\overrightarrow{b_1}$ satisfying the above condition is the reciprocal lattice vector space. In this space, the Laue condition is satisfied and each point represents the possible momentum transfer. And usually the reciprocal lattice vector in this space is denoted by $\vec{G}$.

Reflection high energy electron diffraction

RHEED is a typical tool used for *in situ* film characterization of MBE and PLD. It gives information such as reconstruction and morphology of the film surface through diffraction pattern made by striking high energy electrons on the surface [56,63]. It is a tool that is compatible with ultrahigh vacuum and has a high surface sensitivity that enables real time measurement during film growth. The following figure is a schematic diagram of RHEED geometry.

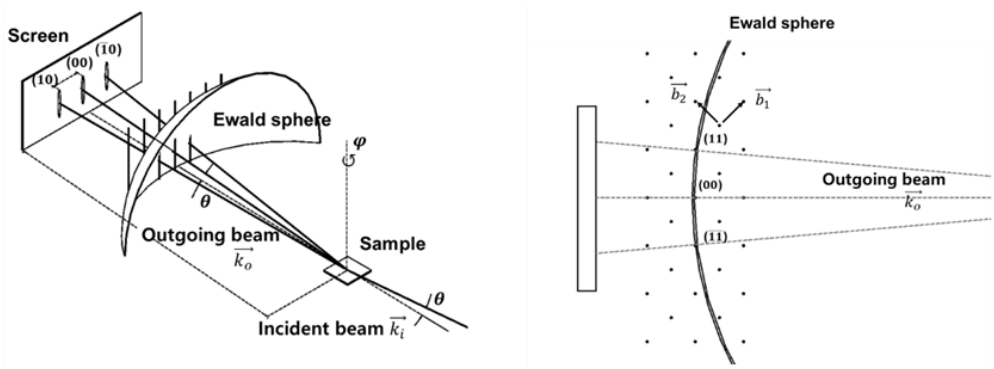

Figure 2.4: RHEED geometry: (a) Schematic illustration of geometry of RHEED (b) Top view of Ewald sphere construction with $\pi/4$ rotated beam direction with respect to (a)

Electrons from the RHEED gun are directed at the sample with a small incident angle (usually less than 3°). There is a phosphor screen opposite to the electron gun. The screen is intended to show the diffracted pattern and should be kept away from the sample so as not to interfere with the deposition. Emitted electrons are usually accelerated at an energy of 10 to 50 keV. Due to the low angle of incidence in this energy region, the penetration depth of electrons is only a few atomic layers. The incident wave vector of electrons $\overrightarrow{k_i}$ has the following magnitude and the wave length of the electron corresponding to the energy is as follows.

$$k_i = \frac{1}{\hbar}\sqrt{2m_0E + \frac{E^2}{c^2}} \ , \qquad \lambda(\text{Å}) = \sqrt{\frac{150}{E(eV)}} \tag{2.17}$$

Where E is relativistic energy, Relativistic effects are often neglected, since relativistic corrections are about 3% at electrons energy with 20 keV. Since RHEED is a surface-sensitive tool, it only probes a few atomic layers. So from a diffraction point of view, the sample can be seen as a crystal surface that repeats indefinitely in the x-y plane. And the periodicity in the z direction, which is the direction perpendicular to the sample, can be ignored. In this geometry, $\overrightarrow{b_3}$ is close to zero, thus becoming an near continuous reciprocal rod. The in-plane component of the reciprocal vector $\overrightarrow{G_\parallel}$ combined as an integer multiple of the above vector is as follows.

$$\vec{G} = \overrightarrow{G_\parallel} + \overrightarrow{G_\perp}, \qquad \overrightarrow{G_\parallel} = h\overrightarrow{b_1} + k\overrightarrow{b_1} \tag{2.18}$$

Where *h* and *k* are integers and $\overrightarrow{G_\perp}$ is a continuous vector. RHEED diffraction occurs when the difference between the momentum of the incoming beam and the momentum of the outgoing beam is equal to the reciprocal lattice vector.

$$\overrightarrow{k_o} - \overrightarrow{k_\iota} = \vec{G} \tag{2.19}$$

Where $\overrightarrow{k_o}$ and $\overrightarrow{k_\iota}$ are the wave vectors of outgoing and incident beams. Imposing elastic scattering condition yields that $|\overrightarrow{k_\iota}| = |\overrightarrow{k_0}|$. These kinematic elastic scattering conditions can be represented geometrically by Ewald sphere construction [69].

The starting point of the wave vector $\overrightarrow{k_\iota}$ of the incident electrons is placed at the reciprocal lattice rods, and the Ewald sphere is defined as a circle whose radius is $|\overrightarrow{k_\iota}|$, centered on the starting point of $\overrightarrow{k_\iota}$. The above diffraction condition is satisfied by the

outgoing wave vectors $\overrightarrow{k_o}$ when the Ewald sphere intersects the reciprocal lattice rods. That is, $\vec{G}$ determined by the crystal structure of the sample is a set of possible momentum transfer. The lattice constant determination using RHEED is actually understood in the following way. The lateral component of the outgoing wave vector in the previous geometry is as follows.

$$k_{ol} = |k_i| cos\theta sin\varphi \tag{2.20}$$

The following conditions are satisfied by the Bragg's scattering condition.

$$\frac{n}{d_l} = \frac{1}{\lambda}(cos\theta sin\varphi) \tag{2.21}$$

Where *n* is the reflection order and d_l is the lateral lattice constant of the beam. $sin\varphi$ is given as the ratio of the sample screen distance to the lateral distance between (h0) rods at screen. The lateral distance between the spots is the inverse of the atomic spacing. And also surface reconstruction can be seen in RHEED as a spot with a smaller spacing period

Ideally, RHEED spots will exist in a sharp spot on the Laue circle if the surface is infinitely large, flat, and has a perfectly crystallized surface without any other disorder. But in reality, it looks a little different. First of all, technically non-monoenergetic electrons make the Ewald sphere into a shell shape so that sharp spots are blurred. And because of the limitations of detecting technology, the spot may look broad. Other than that. If there are many atomic steps on the vicinal surface, the spot looks a little longer in streak form because of the grating in the step. When 3D growth occurs, quantized momentum transfer occurs in the z direction and transmission spots appear on the screen. And on the polycrystalline or textured surface, the pattern appears as a ring.

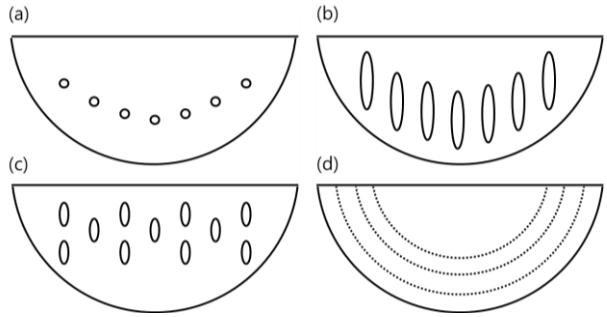

Figure 2.5: Typical RHEED patterns: (a) ideal prefect crystal, (b) smooth surface with atomic steps, (c) diffraction from 3D island, (4) randomly oriented polycrystalline or textured surface.

The most practical use of RHEED as an in-situ surface analyzer is the oscillation of diffraction spot intensity as the thickness of the deposited film increases. At the beginning of the 1980s, it was reported that the Auger electron spectroscopy signal oscillates with the increase of the film thickness in the epitaxial growth of the metal thin film [70]. Then Harris found in the MBE experiments of GaAs that the RHEED intensity oscillated with the thickness and coincided with the period in which the period covered the crystal surface [63]. Since then, kinematic approximation or step density model has been used to explain this periodic behavior. The following is the RHEED intensity obtained from the kinematic approximation.

$$I = I_0[\theta^2 + (1-\theta)^2 + 2\theta(1-\theta)\,cos(q_z d)] \tag{2.22}$$

Where I_0 is the original intensity, θ is the coverage and d is the lateral atomic spacing. And q_z is the incidence angle dependent momentum transfer to surface normal direction. The incidence angle dependence gives the path difference of the scattered beam in the upper and lower layer, and the RHEED oscillation differs with the resulting phase difference. During the periodic repetition of 2D nucleation and growth, the step density is

increased and decreased periodically on the surface. Since electrons are easily scattered at the step edge, the intensity of the specular spot oscillates periodically. This allows us to measure growth rate and is the most characteristic feature of RHEED.

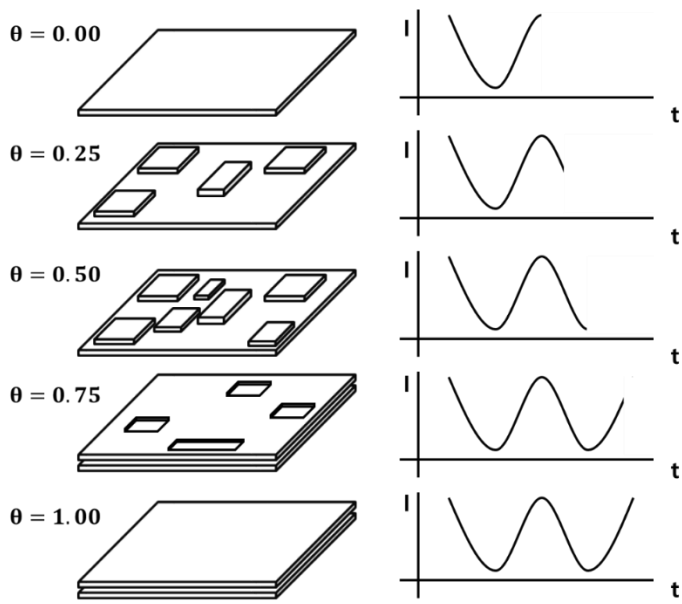

Figure 2.6: Simple illustration of RHEED oscillation as function of coverage

2.5 Low Energy Electron Diffraction

LEED is also a method of in-situ determining the crystal structure of the surface using diffraction of electrons. In this method, electrons with a low energy, typically 20 to 200 eV, are incident perpendicular to the surface. The incident electrons are scattered by the atoms on the surface and the diffraction pattern is imaged on the photosensitive screen. The de Broglie wavelength of the electron corresponds to about 1 Å (1.2 Å at 100 eV) or less, as shown in the above equation, and is suitable for resolving the atomic arrangement and

surface reconstruction. Also, since the elastic mean free path is about to several Å, it is sensitive to probe top most layer. In LEED measurement, reciprocal lattice rods satisfying the Laue condition intersect the Ewald sphere [69]. The diffraction condition is satisfied at a point in the momentum space. The difference from RHEED is that the geometry of the Ewald construction due to the normally incident electrons is as follows.

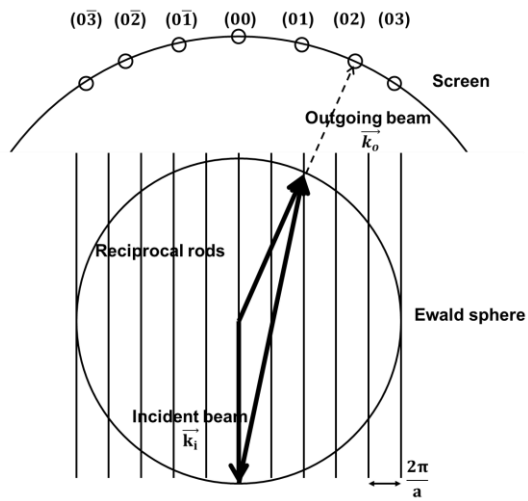

Figure 2.7: Ewald construction in LEED

In RHEED, the Ewald sphere has a large radius because it accelerates to more than 10 keV and a low grazing angle to the sample. Therefore, only a few of the Laue zones that reciprocal rods cross are displayed on the screen, and only a part of the reciprocal lattice space near the incidence direction is measured. In LEED, on the other hand, the radius of Ewald sphere is comparable to the spacing of reciprocal lattice rods. For example, referring to the above equation, if the incident energy of the electron is 100 eV, the radius of the Ewald sphere is 4.8 $Å^{-1}$. The Brillouin zone of all materials with crystalline nature can be projected in LEED. Therefore, it is good to determine full symmetry in all directions.

2.6 Scanning Tunneling Microscopy

Since the development in 1981 by G. Binnig and H. Rohrer, scanning tunneling microscopy (STM) and spectroscopy (STS) have revealed various surface phenomena and electronic structures in various systems on atomic scale [71]. The STM consists of a tip and a sample, the geometry and electronic structure is mapped at the atomic level by the tunneling current between the tip and sample. And the piezo motor can move metallic tip with the resolution of the sub angstrom.

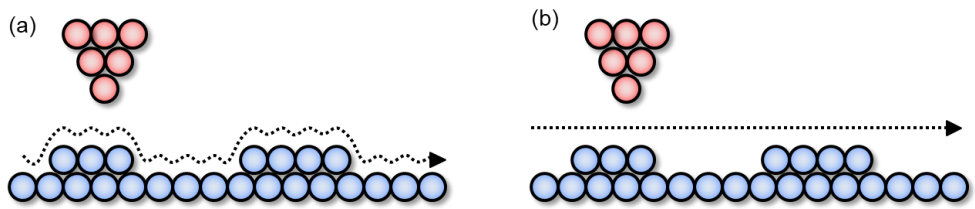

Figure 2.8: STM operation mode: (a) Constant current mode (b) Constant height mode

STM records topographic information in two operation modes. It is constant current mode and constant height mode. Constant current mode is commonly used mode, in which the feedback circuit constantly adjusts the tunneling current between the tip and sample while recording the height of the tip. In this mode, the trajectory of the tip traces the constant DOS of electron. Therefore, in this mode, tip height is recorded on the sample surface. On the other hand, the constant height mode is mode of recording the tunneling current while keeping the height of the tip constant. The scan is faster than the constant current mode because it does not need feedback. But in constant height mode, the tip has the potential to crash when encountering an obstacle, so this mode operates when scanning a flat narrow area.

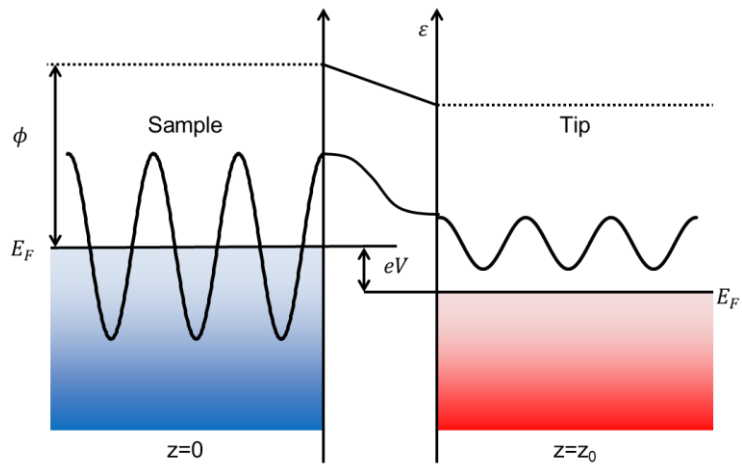

Figure 2.9: Schematic view of tunneling between sample and tip

Now, to understand the working principle of STM, tunneling phenomenon between tip and sample will be discussed, based on Bardeen's transfer Hamiltonian approach. He divided the total system into two subsystems, tip and sample, described by the wave functions ψ_μ and ψ_ν, respectively, solution of the Schrodinger equation of subsystem. The transferring rate between subsystem was calculated by time dependent perturbation theory [72]. The tunneling matrix M is governed by the overlap integral of the two subsystems and can be written as:

$$M_{\mu\nu} = \frac{\hbar^2}{2m}\int d\vec{S}\cdot\left(\psi_\mu^*\nabla\psi_\nu - \psi_\mu\nabla\psi_\mu^*\right) \tag{2.23}$$

This equation is the integral of the current operator with respect to the surface, and the integral area is any surface separating the two subsystems. The transition rate between them is as follows according to the Fermi Golden rule.

$$w = \frac{2\pi}{\hbar}\left|M_{\mu\nu}\right|^2 \delta(E_\mu - E_\nu) \tag{2.24}$$

The δ function implies an elastic tunneling process. Now, with given bias V, the tunneling current is:

$$I = \frac{4\pi e}{\hbar}\int_{-\infty}^{\infty}\left|M_{\mu\nu}\right|^2 \rho_s(E_F - eV + \varepsilon)\rho_t(E_F + \varepsilon)\cdot[f(E_F - eV + \varepsilon) - f(E_F + \varepsilon)]\, d\varepsilon \tag{2.25}$$

Where $f(E) = \{1 + exp[E - E_F/k_BT]\}^{-1}$ is the Fermi distribution function and ρ_s and ρ_t are the density states of the electrodes. And at low temperature limit, that is, when k_BT is less than energy resolution, the tunneling current can be written simply as follows.

$$I \approx \frac{4\pi e}{\hbar}\int_0^{eV}\left|M_{\mu\nu}\right|^2 \rho_s(E_F - eV + \varepsilon)\rho_t(E_F + \varepsilon)\, d\varepsilon \tag{2.26}$$

In Bardeen's formalism, the current equation in summation form is:

$$I = \frac{4\pi e}{\hbar}\sum_{\mu\nu}\left|M_{\mu\nu}\right|^2 f(E_\mu)[1 - f(E_\nu - eV)] \tag{2.27}$$

At the low temperature limit, $k_BT \ll 1$, the tunneling current is:

$$I = \frac{4\pi e^2 V}{\hbar}\sum_{\mu\nu}\left|M_{\mu\nu}\right|^2 \delta(E_\mu - E_F)\delta(E_\nu - E_F) \tag{2.28}$$

Now, in order to obtain the tunneling matrix, the wave function of the sample and the tip is approximated by realistic approximation [73,74]. The surface wave function of the sample is assumed as follows.

$$\psi_\nu = \frac{1}{\sqrt{\Omega_S}} \sum_{\vec{G}} a_{\vec{G}}\, exp\left[\sqrt{\kappa^2 + \left|\vec{K}_{\vec{G}}\right|^2} \cdot z\right] exp[i\,\vec{K}_{\vec{G}} \cdot r] \tag{2.29}$$

Where Ω_S is the volume of the sample, $\kappa = \sqrt{2m\phi/\hbar}$, ϕ is work function in eV, and $\vec{K}_{\vec{G}} = \vec{K}_{\parallel} + \vec{G}$. $\vec{K}_{\parallel}$ is the surface Bloch vector and $\vec{G}$ is the surface reciprocal lattice vector. The wave function of the tip is approximated as s-wave and is written using a solution of spherical potential well with a radius R as follows:

$$\psi_\mu = \frac{1}{\sqrt{\Omega_T}} C_T \kappa R \cdot e^{\kappa R} \cdot \frac{e^{-\kappa|\vec{r}-\vec{r_0}|}}{|\vec{r}-\vec{r_0}|} \tag{2.30}$$

Where Ω_T is the volume of the tip. Now, we substitute these wave functions and obtain the tunneling current as follows.

$$I = \frac{64\pi^3 e^2 V \phi^2 R^2 e^{2\kappa R}}{\hbar \kappa^4} \sum_{\mu} \frac{\delta(E_\mu - E_F)}{\Omega_T} \cdot \sum_{\nu} |\psi_\nu(\vec{r})|^2 \delta(E_\nu - E_F)$$
$$I \propto \sum_{\nu} |\psi_\nu(\vec{r})|^2 \delta(E_\nu - E_F) \equiv \rho(\vec{r}, E_F) \tag{2.31}$$

From the above equation, it can be seen that the tunneling current is proportional to the local density of state. The tunneling current between the superconductor and the normal metal is expressed as Hamiltonian using the quasi particle operator discussed in the previous section [75].

$$I = \frac{4\pi}{\hbar}\int_{-\infty}^{\infty} dE_k N_S(E_k)\int_{-\infty}^{\infty} d\xi_q N_q(0)\left\{|\langle q|H_T|k\rangle|^2 f(E_k)\big(1-f(\xi_q)\big)\delta\big(\xi_q - E_k - eV\big)\right.$$
$$\left. - |\langle k|H_T|q\rangle|^2 f(\xi_q)(1-f(E_k)\delta\big(\xi_q - E_k - e|V|\big)\right\} \tag{2.32}$$

When the matrix component is calculated, the tunneling current equation is simplified as follows.

$$I = \frac{4\pi e}{\hbar}\left|M_{kq}\right|^2 N_q(0)\int_{-\infty}^{\infty} dE_k N_s(E_k)\{f(E_k) - f(E_k + eV)\}$$
$$= G_{NN}\int_{0}^{e|V|}\frac{E}{\sqrt{E^2-\Delta^2}}\{f(E) - f(E+eV)\}\,dE \tag{2.33}$$

So far the tunneling phenomenon between tip and sample has been reviewed. Using this tunneling current, STM obtains topographic information of the sample surface. In addition, STM has a mode to measure dI/dV while sweeping the voltage. This technique is called STS and reveals the density of state information of the sample. The STS utilizes a lock-in technique to reduce noise in the dI/dV measurement. When a small modulation AC voltage is applied to the voltage, the response is as follows.

$$I(V + A\sin\omega t) = I(V) + \left.\frac{dI}{dV}\right|_{V_0}\cdot A\sin\omega t + \frac{1}{2}\left.\frac{d^2I}{dV^2}\right|_{V_0}\cdot(A\sin\omega t)^2 + \cdots$$
$$\approx I(V) + \left.\frac{dI}{dV}\right|_{V_0}\cdot A\sin\omega t + \frac{1}{2}\left.\frac{d^2I}{dV^2}\right|_{V_0}\cdot A^2\left(\frac{1-\cos 2\omega t}{2}\right) \tag{2.34}$$
$$+\cdots$$

The lock in technique is a frequency-sensitive measurement technique that can measure the component of oscillating ω period. Therefore, measuring the coefficient of the first harmonic ω period yields the differential conductance dI/dV. Similarly, the second derivative can be measured by measuring the second harmonic 2ω term.

Chapter 3. Design and Construction of Laser-MBE Combined with STM System

3.1 Introduction

Since the invention of the late 1960s, MBE has proven to be a powerful way to grow a variety of thin film novel materials [61]. This technique is versatile enough to study semiconductors with atomic level of precision, study various nanostructures, and even grow magnetic and superconducting materials to study physics. Invented in 1981, STM is huge triumph in surface physics research [71]. This microscope can explore the surface of materials at an atomic scale and reveal the electronic structure with the STS technique. The combination of MBE and STM offers a number of advantages in that an atomically clean and sharp surface grown with the MBE can be studied directly into STM without degrading the quality that would inevitably encounter during transfer process. Recently, a lot of research has been going on with the combination of these two, which is raising the expectation that STM will study more novel quantum phenomena [76].

The high-temperature superconductivity field is one of the most attractive fields in the field of condensed materials physics, and many studies have been made using STM. Research on these materials using STM usually proceeds by cleaving the bulk grown sample in UHV [77–89]. Often, samples are also cleaved at low temperatures to prevent diffusion. Because the majority of high-temperature superconductors have complex compositional chemical formulas which is more than ternary, it is not easy to grow and measure in situ using MBE. In addition, the cleaved samples are only available in weakly-bound, layered materials and have the disadvantage of leaving unwanted cracks and

residues in the cleaving process [90]. This method is a somewhat less reproducible technique that requires trial and error.

An alternative approach to overcome disadvantages of cleaving sample study is the combination of Laser-MBE and STM. Laser-MBE is a thin-film deposition method using PLD technique, which is used to make functional metal oxide and ferroelectric materials with atom-level precision. The combination with STM makes it possible to perform *in situ* studies on complex compositional regions that MBE does not cover. Taking the above mentioned points as a starting point and motive of the study, this chapter deals with the design and construction of a laser-MBE combined with STM system. The author discussed design considerations and ideas in this chapter. The details of the construction are presented.

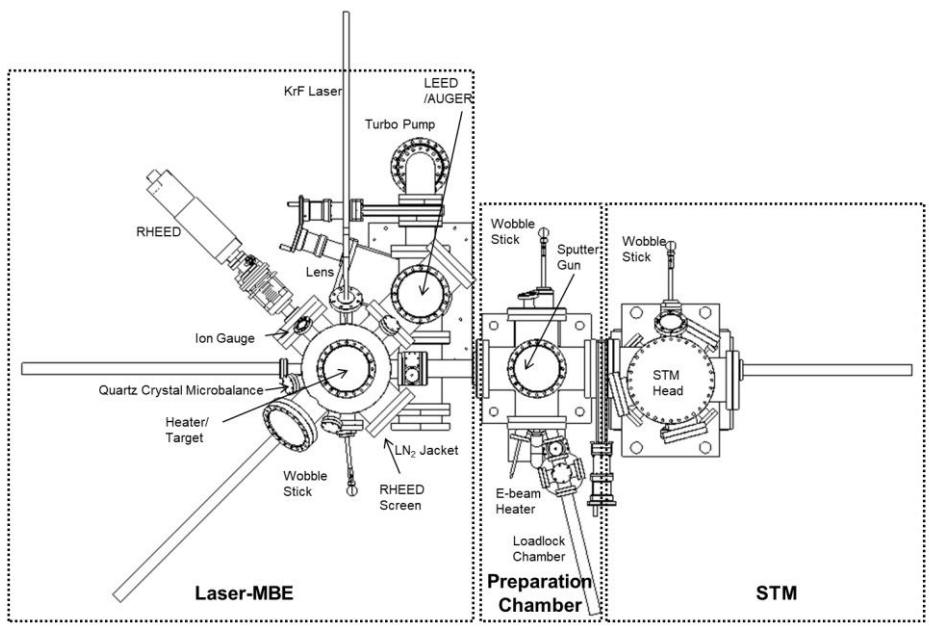

Figure 3.1: Technical drawing of Laser-MBE combined with STM system

The equipment used in the experiment that the author built is shown in the above figure. First, the growth chamber, Laser-MBE, is discussed on a component-by-component basis. And STM and Prep chambers, and the combined total system. The last section discusses the vacuum transfer chamber that allows samples to be transferred to other STM systems in the laboratory

3.2 Laser-MBE

Heater

The heater was designed with the cleanest thin film deposition without contamination as a top priority. First, the emphasis was on reducing heat mass to reduce outgassing at high temperatures. In addition, the parts close to the sample were machined so as not to be bulky with molybdenum. The heater is suspended in a dual shaft manipulator capable of azimuthal rotation and push and pull operation in stages where XYZ motion is possible. This XYZ stage and manipulator were purchased from MDC vacuum product. Push and pull motion is designed to realize tilt motion. Therefore, by using the rotation and tilting operation, it is possible to switch to the RHEED pattern corresponding to the other beam direction during the heating of the sample, and also to measure the desired Laue zone. And because of the XYZ freedom, the sample position is adjustable along with the formation of the plume when laser is ablated.

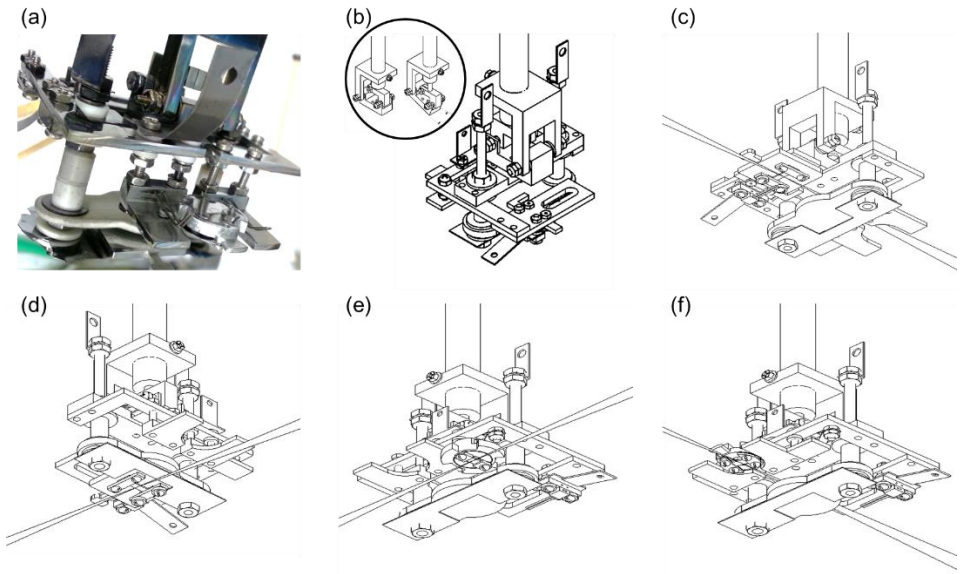

Figure 3.2: Heater design of Laser-MBE: (a) Picture of Laser-MBE heater STM1 type and STM 2/3/4 type samples are mounted. (b) Schematic diagram of heater. Inset shows push/pull motion converted to tilting motion of heater. (c)-(f) Schematic illustrations showing that the RHEED beam path is secured when another type of sample is mounted. (c) resistive heating for STM2/3/4 sample. (d) PBN heating for STM 2/3/4 sample. (e) STM 0 sample. (f) STM 1 sample.

In the heating method, two types of methods are available: DC heating to flow current to a sample when the substrate is a semiconductor type, and heating the sample using pyrolytic boron nitride heater of Boraelectric Co. It was also a design consideration to allow thin film deposition in other types of STM sample holders. STM currently used in the laboratory uses three kinds of sample holders, and these sample holders are designed to be capable of heating and thin film deposition in the growth chamber. Also, it is possible to ensure real time RHEED monitoring by securing the beam path even when thin film deposition using other sample holders.

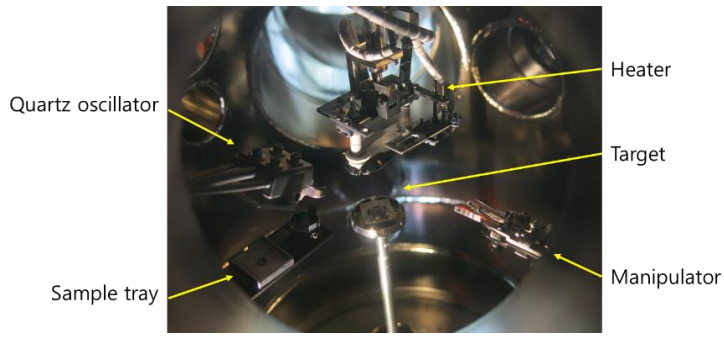

Figure 3.3: Inside of Laser-MBE Growth chamber

PLD setup

The PLD setup is shown in Figure 3.6. In this study, a COMPEX 102 KrF excimer laser from Lambda Physic was used. The laser has a specification with a wavelength of 248 nm, a pulse duration of 30 ns, an average power of 6 W and a maximum repetition rate of 20 Hz. The 248 nm used in the experiment has a photon energy equivalent to 5.00 eV. Depending on the material, the wavelength of the laser can also be a consideration. Since the photon energy is absorbed by the target and laser ablation occurs, the photon energy is larger than the gap of the target so that the absorption is easy. Therefore, when the material is a wide gap material, a difficult situation may occur.

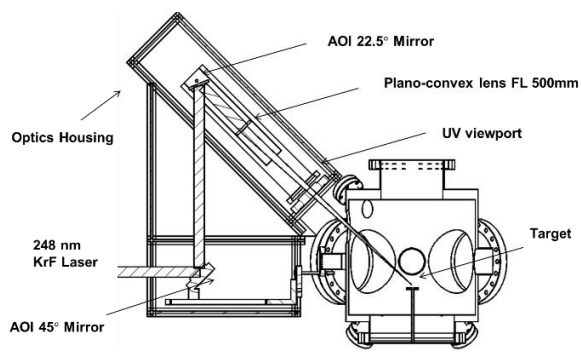

Figure 3.4: PLD Laser optics and alignment apparatus

The beam from the excimer laser is reflected in a mirror with an angle of incidence (AOI) of 45° and a mirror with AOI of 22.5°, and is converged inside the chamber through a plano convex lens with a focal length of 500 mm. Note that the focal point of the lens just above the target increases the non-uniformity of the beam energy profile. To overcome this problem, illumination on the image plane of the beam geometry is used in this setup. The position of the lens and the target can be obtained by a thin lens formula using the demagnification ratio corresponding to the desired fluence. The viewport, which the laser passes into the chamber, is UV grade fused silica lens. The laser alignment apparatuses are covered with a plastic housing. This firstly reduces the risk of eye damage, and secondly it protects the lens and mirror from dust.

Because the target has the same shape as the STM sample holder, it can be loaded through the load lock chamber without breaking the vacuum. The target stage is rotating to prevent overheating specific spot and to deposit uniformly. The difference from other PLD systems is that they can move in the z-axis direction. This z-motion freely changes the distance between the sample and the target, and can prevent interference with evaporator. The rotation of the target stage is controlled by a stepper motor. The stepper motor was hardware controlled with Easy Driver and Arduino uno, and the software control was done by Labview.

High pressure RHEED

PLD is a technique of thin film deposition, and it is the most advantageous that it can transfer complex stoichiometry of target to sample. It is also capable of growing complex oxide thin film at high oxygen background pressure. However, it is difficult to use RHEED in O_2 environment because the filament is oxidized and aged in the high-pressure environment and its lifetime is reduced. In this study, differential pumping was used to

lower the pressure around the filament so that real-time RHEED monitoring can be performed even under high-pressure environments [91]. As shown in Figure 3.4, the pressure inside gun is lowered by using second stage differential pumping. The turbo molecular pump lowers the pressure of the gun body with speed of 400 l/s, and the mid stage connected to the gun with ∅2 hole is pumped by a turbo molecular pump with pumping speed 100 l/s. The middle stage is a 300 mm long, 3/8 " OD tube with ∅0.5 hole at the end of the tube to make bad conductance and give a pressure difference to the chamber. In this design, since the e-beam deflection is not available because of alignment of hole and tube, the movement of the RHEED beam is realized through the XY-manipulator.

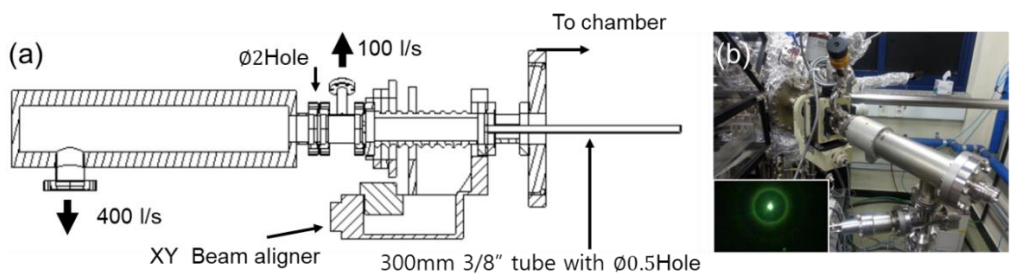

Figure 3.5: Differential pumping for high pressure RHEED: (a) Section view of technical drawing of second stage differential pumping. (b) Picture of growth chamber equipped with homemade high pressure RHEED. Inset shows electron beam passing through two holes.

The system is considered to be able to grow oxide thin film superconductors and functional complex oxide materials at the design stage. These films require a high pressure of oxygen or buffer gas environment during growth, but pressure of the filament in RHEED must be kept low enough to allow operation. The following table summarizes the growth conditions for common oxide films.

Material	Temperature (℃)	P_{O2} (mTorr)	Reference
$YBa_2Cu_3O_7$	800	150 - 220	[92–94]
$La_{2-x}Sr_xCuO_4$	780	10 - 300	[95]
$La_{2-x}Ba_xCuO_4$	770	225	[96]
$LaAlO_3$	800	10	[97]
$SrTiO_3$	800	100	[98]
TiO_2	500	35	[99]

Table3.1: Growth conditions of common oxide films

RHEED system were equipped from STAIB's EK-315-RMG. Our RHEED has a maximum acceleration voltage of 12 keV and the filament operates at pressures below 10^{-5} Torr. The pressure in the filament maintains 8.6×10^{-6} Torr when the growth chamber is maintained at 200 mTorr. A final consideration is the attenuation of the beam. If the mean free path of the beam is comparable to the distance between the RHEED and the screen, the attenuation of the beam intensity along the distance should be considered. According to G. Rijnders [100], in an oxygen environment of 200 mTorr, the travel distance of 15 cm has an attenuation value of about 0.1.

$$I = I_o Exp[-\frac{x}{l_{MFP}}] \tag{3.1}$$

The mean free path is inversely proportional to the product of the total scattering cross section and the molecular density. The extension tube was as close as possible to the sample, and the phosphor screen was also close to the sample, as long as it did not interfere with deposition and manipulation. The performance was confirmed in an oxygen environment

with a RHEED pattern of 200 mTorr when growing high temperature superconductor, Y123.

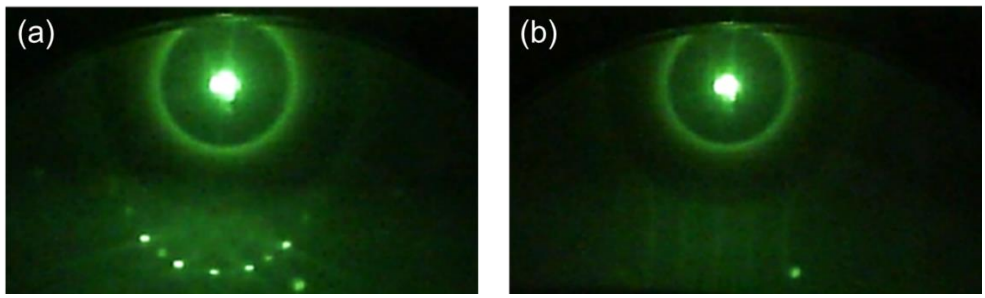

Figure 3.6: RHEED pattern taken on $YBa_2Cu_3O_7$ (Y123) on $SrTiO_3$ (100): (a) Before deposition. (b) 2000 pulse of Y123 deposited on STO substrate.

LEED/Auger

The LEED / Auger equipment used to determine the surface crystal structure of the substrate or grown thin film was SPECTALEED from Omicron. A sample was placed in the LEED optics using a magnetic translator and a precision port aligner, so that images could be obtained. Since LEED does not actually produce perfect elastic scattering, it is possible to suppress the inelastic scattering by giving the grid an adjustable negative voltage. In addition, to increase the contrast, a positive high voltage is applied to the screen to obtain a sharp image. The following figure shows LEED optics and LEED of 7×7 surface reconstruction of Si (111) obtained by repetitive resistive flash.

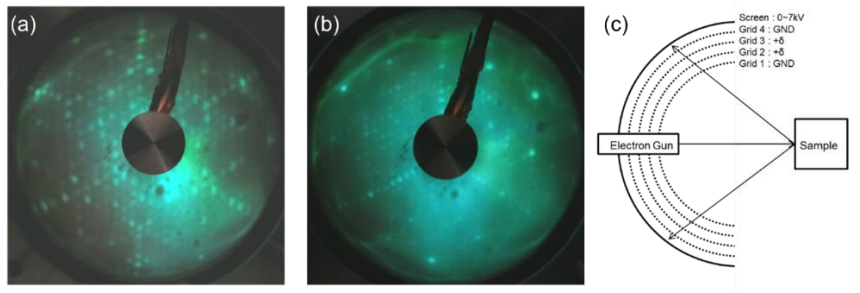

Figure 3.7: LEED images and LEED Optics: (a) LEED pattern showing 7×7 reconstruction Si (111) obtained at an energy of 60 eV and (b) 120 eV. (c) A schematic diagram of LEED optics. This scheme applies same to AES.

In Auger process, the core electron is removed by scattering with incident electrons (or photons), and a hole is created. If the energy gain resulting from filling the hole with the outer shell electron is greater than the bond energy of the second outer shell electron, the process occurs as it emits with a certain energy. The energy spectrum and intensity of the emitted electrons correspond to the fingerprint of each material. And since electrons have a short mean free path in solids, they are a useful tool for studying the chemical composition of surfaces. This technique can be used without changing the LEED optics mentioned above. The voltage at which the accelerating voltage was 200 eV maximum at LEED was changed to 3 keV at Auger. There are techniques such as cylindrical mirror analyzer and retarding field analyzer that analyze the spectrum of emitted electrons by energy. Here, we adapted the RFA method. When a retarding field is applied, electrons with weaker kinetic energy than the field are suppressed, and electrons with stronger kinetic energy than the field can reach the detector. The energy derivative of number of the electrons detected by sweeping the field is the spectrum of the Auger electron. The author used the lock-in technique to obtain derivative. That is, small AC component is added to

the DC retarding field to obtain the first harmonic response, the derivative. This method was realized by the Labview program.

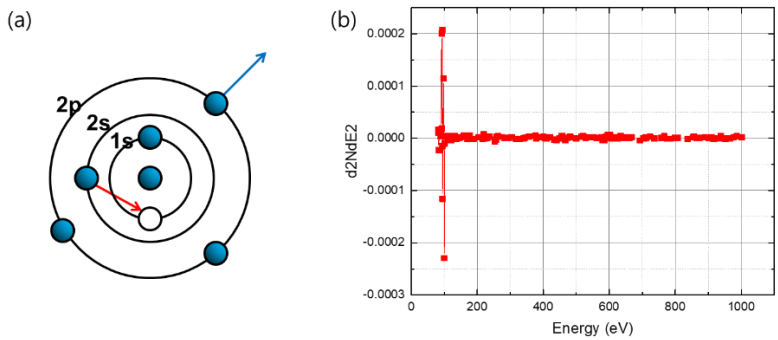

Figure 3.8: (a) The illustration of the Auger process and (b) the Auger electron spectrum of Si: Clean Si (111) surface is confirmed by sharp d^2N/dE^2 peak at 92 eV.

Evaporators

An evaporator or effusion cell is apparatus to deposit the desired material in MBE. In crucible type evaporator, crucible containing the material is wound with tungsten filaments, which are designed to flow current through the filament and raise the temperature of the material inside the crucible. The heated substance is exiting through an orifice in front of the cell. The flux is controlled by the power of the filament and follows the effusion equation. In addition to the crucible type, there are cells that match the properties of each material. An e-beam evaporator may be used for materials that require refractory metals or evaporating temperatures above about 1000 degrees Celsius.

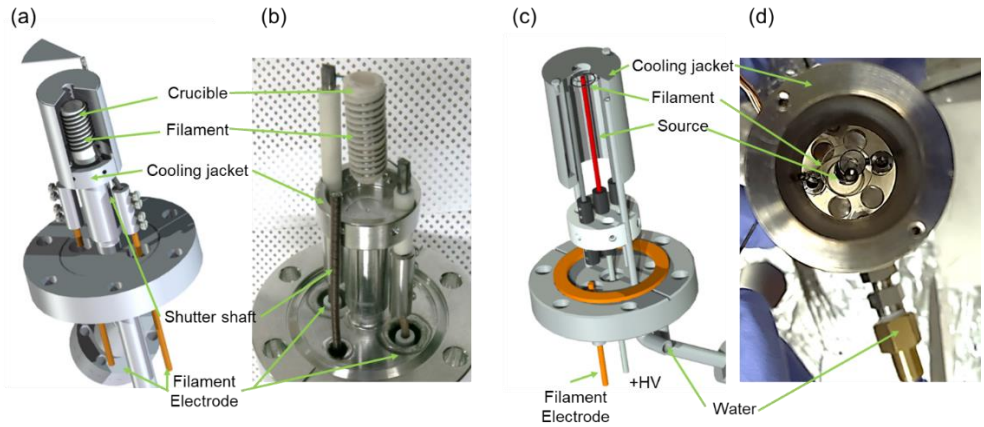

Figure 3.9: Two types of evaporator: (a) is CAD of crucible type evaporator. (b) is picture of homemade evaporator based on (a). (c) is CAD image of e-beam type evaporator. One side of the filament is grounded. The source is connected to the + HV terminal by thin tungsten wire to prevent thermal escape. (d) is a top view of homemade e-beam source based on (c).

Although not used in this experiment, there are other types of sources available. Materials such as As or P that do not decompose well into monomer when heated are used in a multi zone heating technique called a cracker cell. In addition, if you want to deposit materials in an N_2 or O_2 activated environment, you can make them reactive with the help of RF plasma. The vapor pressure curve of the elements used in this setup is as follows. The typical MBE growth is 10^{14}~10^{15} /cm^2·s which corresponds to 10^{-4}~10^{-6} Torr in beam equivalent pressure.

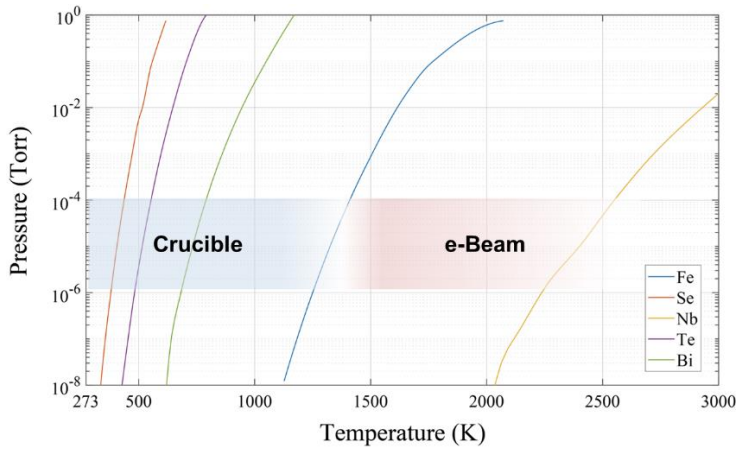

Figure 3.10: Vapor pressure curve of elements used in this study: the crucible type is used for the material evaporable at low temperature and the e-beam type is used for the high temperature material. In this study, the iron source employed an e-beam type.

Chamber and Vacuum

The chamber for Laser-MBE is basically designed to perform high-quality MBE growth and PLD growth at the same time. The main chambers were made of stainless steel 304, with low outgassing, so that clean samples could be produced. The chamber was rinsed with detergent and cleaned with solvent before vacuum pumping. In addition, the inner parts are used only UHV compatible materials, and all screw, taps and voids were vent hole designs.

From Figure 3.6, there are 13 evaporator ports that are oriented to the center of the chamber. The bottom center port is for the rotating PLD target, so a maximum of 12 evaporator sources can be installed. Since the sample is supposed to grow in the center of the chamber, the ports where the KrF lasers enter are positioned with the port facing 40 mm from the center. Some ports do not interfere with the laser ablation, which allows

simultaneous operations of PLD and MBE. For ease of operation, the 8-inch viewport is mounted diagonally, and Huntington's wobble stick is mounted on a 4.5" port for maximum 16° angles.

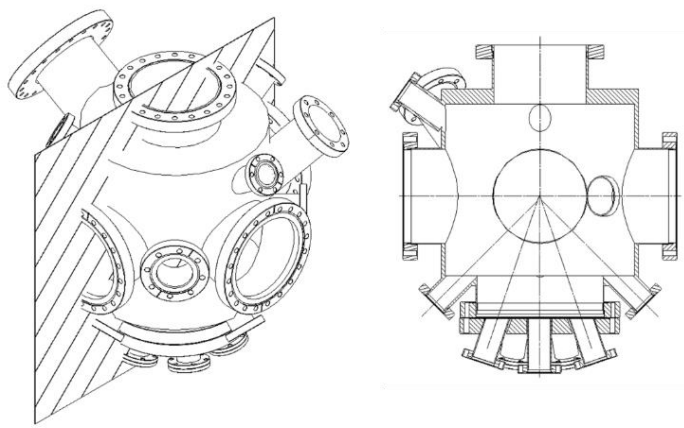

Figure 3.11: CAD image and cross-sectional technical drawing of growth chamber

The heater is suspended in the 8" top flange. The upper 2.75" ports were equipped with quartz crystal microbalance to measure the film deposition rate, leak valve for the O_2 supply, and Bayard Alpert type ion gauge to measure vacuum pressure. The high pressure of the mTorr order was also measured using a capacitance manometer.

Ultra high vacuum is maintained by titanium sublimation pump and 240 *l/s* ion pump after baking the chamber. Liquid nitrogen shrouds around the TSP cryo-pump the outgassing, especially from high temperature sources or samples.

Deposition calibration

In this study, quartz crystal microbalance was used to measure the flux of the MBE source. The principle of operation is that high Q quartz resonator disks measure the mass

addition by frequency shift. Since this is a measure of mass change, the densities and Z-ratios of the material must be entered before measurement. This measurement does not take into account the sticking coefficient for each material or re-evaporation when growing the actual sample, but it provides powerful performance in calibration. It is mounted on the bellows and is designed to move alternating between sample position and retracted position.

As mentioned in the previous chapter, RHEED not only measures the crystal structure of the surface and reconstruction but also measures the deposition rate through the intensity oscillation of the specular spot. The RHEED intensity is weakened by diffuse reflection at the terrace edge. Therefore, there is no oscillation in the step flow mode in which the step densities do not change during growth. In this study, we developed Labview program that extracts the RGB values of desired spot, converts it into an intensity, and records it, while monitoring the pattern in real time with a CCD. The following figure shows the RHEED oscillation of Bi_2Se_3 growth, where each oscillation corresponds to 1 QL growth.

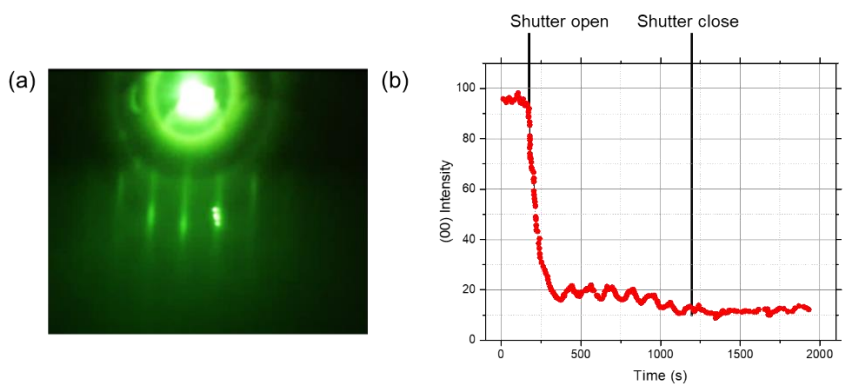

Figure 3.12: RHEED Intensity oscillation of Bi_2Se_3 film: (a) RHEED of as grown Bi_2Se_3 film. (b) Intensity oscillation of specular beam as function of deposition time

A micro patterned grid method was used as an alternative for materials not sticking well to QCM or for materials that do not grow in FM mode. You can estimate the deposition rate by the height difference between the flat top and the bottom using an AFM after depositing a micro grid on the sample. In this study, the calibration of the films deposited using PLD technique was performed by this method.

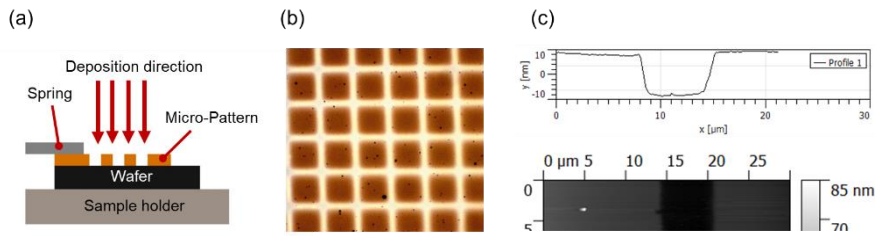

Figure 3.13: Deposition calibration of $Ba(Fe_{1-x}Co_x)_2As_2$ using micro patterned grid: (a) Schematic drawing of deposition rate calibration, (b) Optical microscope image of deposited pattern with size of 20 µm × 20 µm, (d) Height profile measurement by AFM. The rate is then 0.005 nm per pulse with pulse energy 100 mJ.

3.3 Scanning Tunneling Microscopy

Scanner

The scanner is the most important module in the STM where the scanning proceeds by tunneling current between the tip and the sample. The following picture shows the scanner used in this study. For coarse Z and XY movements of the tip we used 1/4" dimeter and 1" length PZT tubes. And piezo disc stack attached to the top of tube controls fine Z motion. This separate z-motion is designed to improve the resolution of z in topography and to

compensate for drift by coarse z. The tip was designed with a magnet to be replaceable on the fine z stack. The piezo tube, disc and tip are mounted in a hexagonal sapphire prism. And a coarse approach is realized by six stacked column walkers attached to the prism. This method is designed by S. H. Pan [101], and details can be found in the corresponding paper. As can be seen, the sapphire prism is supported by the CuBe plate spring at the front of the scanner, and the tension of the spring can be adjusted by four # 0-80 screws.

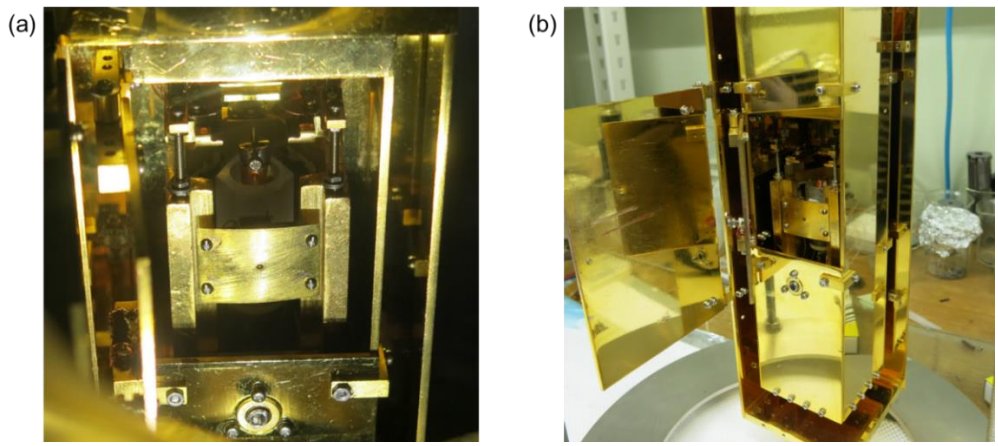

Figure 3.14: Picture of STM scanner: (a) Front view of scanner and (b) without outer shield

Scanner body is made of oxygen free high conductivity (OFHC) copper. The dimensions of the body are 50mm×50mm×80mm, suspended by three Inconel 718 springs. It is also coated with gold to lower the emissivity and prevent temperature rise from external radiation. SmCo magnets are attached to the bottom of the body to damp vibration with eddy current.

Cryogenic

The thermal stability and cooling efficiency of the STM scanner is determined by the thermal shield surrounding it. Here, a dual OFHC copper shield with a hinged door was

used. The inner shield is then cooled by direct contact with the cold tip of the cryostat, and the scanner can make a thermal contact with the bottom set screw when cooling. The low temperature experiment adopted an open cycle cryogenic system called continuous flow. The consumption of helium is 1.5 liters per hour, and a silicon diode is attached to the scanner to measure the temperature.

Preparation chamber

The preparation chamber serves as a connection between the scanner chamber, the laser-MBE growth chamber, and the load-lock chamber where the sample can be loaded, to the gate valve. The chamber is equipped with an e-beam heater and a sputter gun, so the sample and substrate can be cleaned with ion bombardment and annealing.

3.4 Laser-MBE Combined with STM

We integrated the Laser-MBE and STM based on the considerations discussed in the previous section. The picture of the whole system is as follows. In the process of merging, the sample was designed to move freely through the prep, the scanner chamber, and the load-lock using a magnetic transfer arm with a rotating sample tray. Each wobble stick jaw is designed to be universally designed to grab all the samples used in the lab. In addition, LEED / Auger and RHEED are also available for all sample holders.

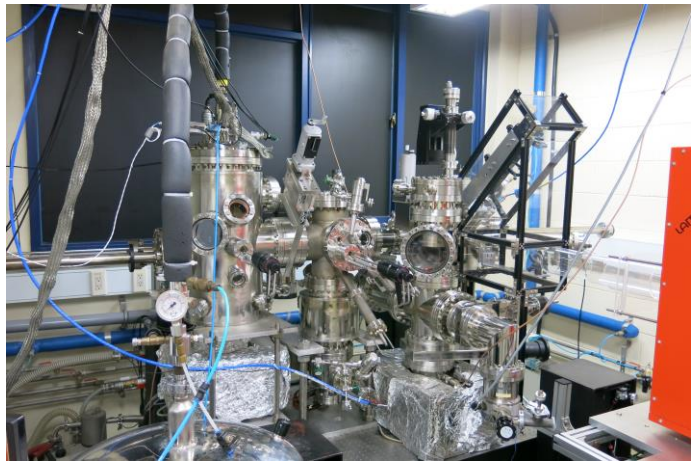

Figure 3.15: Image of Combined the Laser-MBE with STM System

Various thin film samples were grown on the above system. The grown samples were measured in situ and the results are presented here. Figure 3.14 shows the topography image of the samples grown in the Laser-MBE. Each sample was grown by PLD or MBE, and STM measurement confirmed a highly crystalline, contaminated surface. Among these, the growth and measurement of $Ba(Fe_{1-x}Co_x)_2As_2$ and LiFeAs, samples for studying iron-based high-temperature superconductors for initial setup purposes, are discussed in detail in chapters 4 and 5.

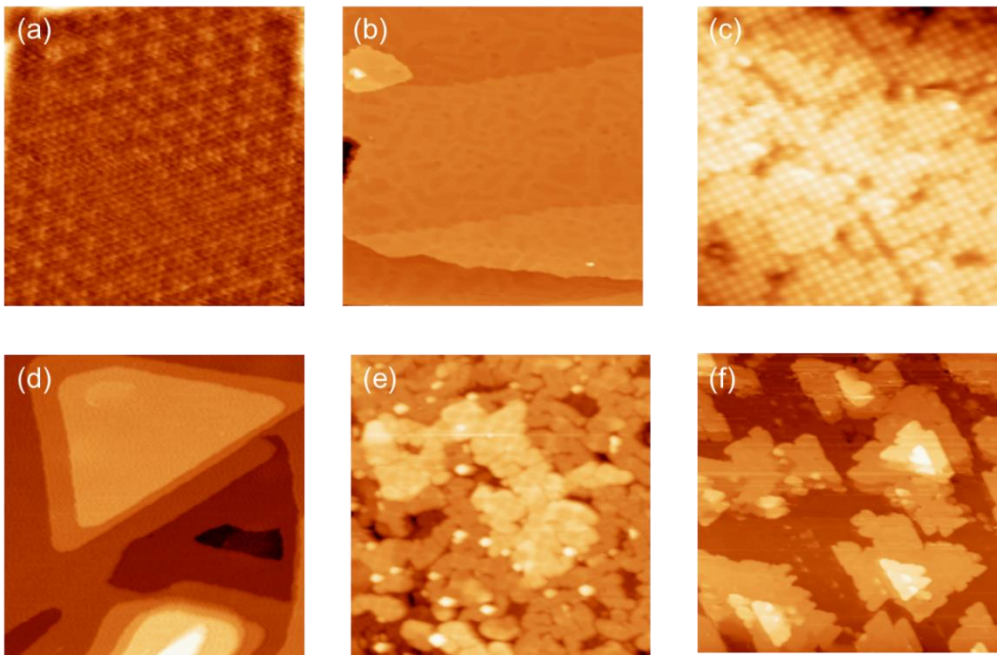

Figure 3.16: Topography of various samples *in-situ* measured by STM in our Laser-MBE setup: (a) $NbSe_2$, (b) FeSe, (c) $BaFe_2As_2$, (d) Bi_2Se_3, (e) LiFeAs, (f) $Bi_2(Se_xTe_{1-x})_3$

3.5 Vacuum Sample Transfer

The vacuum transfer chamber is a portable ultra-high vacuum suit case and is used for sample transfer between UHV systems. Because the pressure of transfer chamber is kept ultra-high vacuum during transfer, the sample can avoid various contaminants, including atmospheric gases. The structure of the vacuum transfer chamber is as follows. A wobble-stick with jaw designed to grab sample holders used in various systems, an 80 l/s Ion pump, a gate valve, a TSP or a non-evaporable getter pump. The grown sample is moved to the transfer chamber attached to the load lock and then transfer chamber is detached. Then, it is docked to the load lock of the system to be moved, then the space between is pumped,

and then the gate valve is opened and transferred to another system. Since all of this procedure is done within a few hours, the sample is kept clean in UHV.

Chapter 4. Pulsed Laser Deposition Growth of Co doped $BaFe_2As_2$ on $SrTiO_3(100)$

4.1 Introduction

The area of high-temperature superconductors was considered mainly possible only in cuprate perovskites until 2006 [31]. However, iron-based superconductors have been extensively synthesized and studied to date, since the Hideo Hosono group reported possible iron-based oxypnictide superconductors [30]. Even this new class of high temperature superconductor includes iron, a ferromagnetic material thought to be far from superconductivity. This class of superconductor has a higher transition temperature than conventional superconductors and has an extremely high upper critical field. These iron-based superconductors have a common FeX (X is pnictogen or chalcogen element) layer and are categorized as '11', '111', '122', '1111' according to their structure. The 122 compounds discussed in this chapter are materials with composition formula of $AEFe_2As_2$, where AE is an alkaline earth divalent ion (Sr, Ba, Ca). Rotter et al., 2008, found a maximum transition temperature of 38 K and '122' began to be studied in earnest [89,102].

Among the 122 compounds, the first reported, and one of the extensively studied, is $BaFe_2As_2$. $BaFe_2As_2$ has a transition temperature of 22 K when optimally doped. Bulk properties of this material have been extensively studied in relation to superconducting properties such as crystal structure, transport properties, magnetic structure and transition, and electron structure. And thin film deposition by PLD technique is well established. Much research has also been carried out on various doping and growth conditions of $BaFe_2As_2$ films.

Superconductivity research using STM gives many insights. Beyond probing the local gap structure at the atomic scale, even QPI technique reveals information about pairing state and symmetry [89,102]. So far, the STM study of $BaFe_2As_2$ has been performed on the surface of cleaved bulk sample [84–87]. The samples produced by the cleave method show the characteristics of the bulk. On the other hand, STM research on thin film $BaFe_2As_2$ films has not been done yet. And superconducting thin films have new physical phenomena different from bulk. Therefore, the thin-film study of Ba-122 is worth investigating using STM.

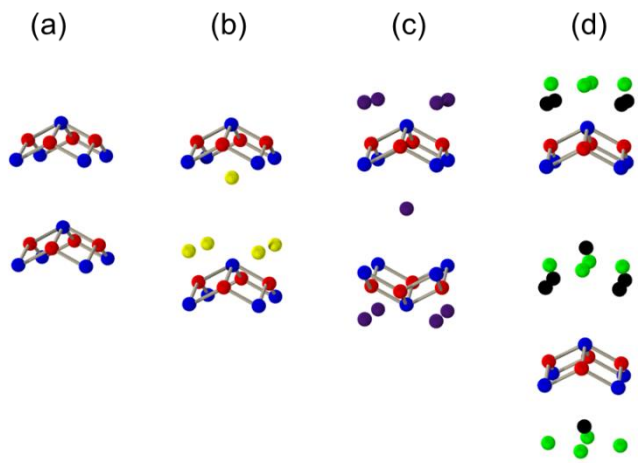

Figure 4.1: Fe-based superconductor family: (a) “11”, (b) “122”, (c) “111” and (d) “1111”

In this chapter we report the growth of $Ba(Fe_{1-x}Co_x)_2As_2$. We present optimization of growth parameter using RHEED, LEED and STM and analyze the morphology corresponding to each condition. The superconducting characteristics will also be discussed using low temperature STM experiments.

4.2 Structural Properties of $BaFe_2As_2$

The structure of the $BaFe_2As_2$ compound is shown in Figure 4.1. It has a tetragonal $ThCr_2Si_2$ structure at room temperature and an interlaced layer between the two FeAs in the unit cell. This intercalated layer serves as a charge reservoir, and adjacent charge reservoir layers have $(a/2, a/2, 0)$ slipped geometry. As in the structure of the FeAs layer in a typical iron-based superconductor, arsenic atoms are alternately located above and below at the center of Fe square net. And adjacent FeAs layers have an inversion symmetry with respect to the center barium plane.

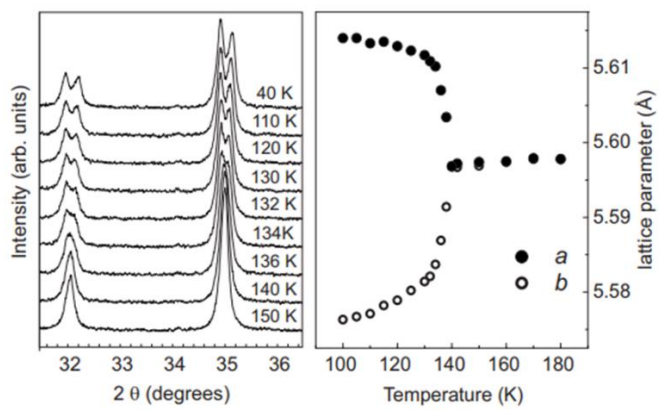

Figure 4.2: Structural phase transition: 110 and 112 reflections are plotted for the change in temperature (Left), and the in-plane lattice parameters a, b change with temperature (Right). The value is multiplied by $\sqrt{2}$ based on the tetragonal phase. image taken from [103]

The lattice constant of $BaFe_2As_2$ has tetragonal crystal structure with a = b = 3.96 Å and c = 12.8 Å at room temperature [103]. And this structure undergoes orthorhombic transition at 140 K. As can be seen in Figure 4.2, the structural phase transition occurs at 140 K with magnetic transition. This structural transition is a phenomenon often occurring in iron-based superconductors except for the '111' structure.

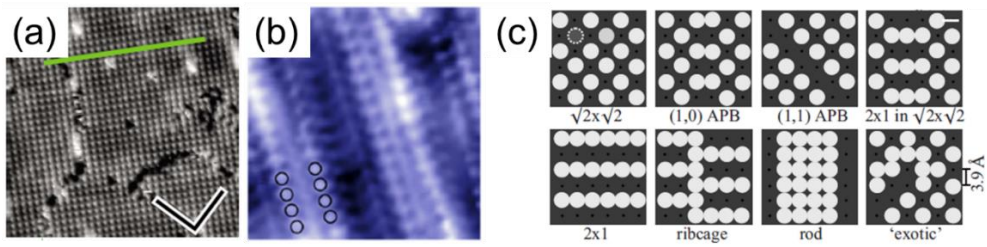

Figure 4.3: Surface reconstructions on cleaved sample: (a) $\sqrt{2} \times \sqrt{2}$ checkerboard, (b) 2×1 stripe and (c) schematic configuration of surface reconstruction. Images taken from [85], [86]

Figure 4.3 shows the previous studies on surface reconstruction of the cleaved sample. The studies using LEED and STM show that the surface reconstruction of cleaved $BaFe_2As_2$ has strong cleavage temperature dependence and the most frequently occurring phase is $\sqrt{2} \times \sqrt{2}$ and 2×1 phase [85,87]. These two reconstructions are known to be metastable. This is because, after warming up, these phase is not obtained even if the temperature is lowered again. $\sqrt{2} \times \sqrt{2}$ and 2×1 reconstruction unit area is $2a^2$, satisfy $1/2$ barium stoichiometry and satisfy charge neutrality. In addition, an antiphase boundary and ribcage pattern, which is represented by the shift of barium over-layer, are occasionally seen on the surface.

The structural properties of thin film $BaFe_2As_2$ are also actively studied. The structural properties of the films are inevitably influenced by substrate. Substrates for epitaxial growth require crystals of the cubic perovskite family with small lattice misfit. Previous studies were done on various substrates mainly using PLD techniques [9,104–108]. c-axis growth has also been reported with epi relation (001) [100] || (001) [100] in LAST and STO, the substrate used in this study. The typical methodology of thin film structural study includes the measurement of the superconducting properties (critical temperature and critical current) due to strain effect or relaxation depending on the thickness of the film.

4.3 Growth Condition of $Ba(Fe_{1-x}Co_x)_2As_2$ on $SrTiO_3(100)$

Substrate

$SrTiO_3$, a perovskite crystal with a lattice constant of 3.905 Å, is a widely used substrate for superconductor film growth. Growth of thin film $BaFe_2As_2$ has also been reported on STO. Considering that the lattice constant of $BaFe_2As_2$ is 3.95 Å, STO with a small lattice misfit is suitable for use as a substrate. As shown in the figure, the STO has a structure in which the SrO plane and TiO_2 planes alternate along the principal axis. The effect of STO termination on growth has been reported in other oxide growths, and therefore well-defined surface treatment is required to obtain reproducible results. Since as-received substrates have not well defined termination, we adopted a recipe that gives TiO_2 termination in STO treatment [109,110]. First, the substrate was rinsed with acetone and isopropyl alcohol and then etched for 5 minutes in NH_4F buffered HF solution adjusted to pH 4.5. This solution dissolves SrO and does not etch TiO_2. Then, after the STO was loaded into the vacuum chamber, annealing several cycles at 1200 °C for 30 minutes at UHV yields a clean, flat and single termination STO with 2×2 reconstruction. This can be seen from the fact that the step height of the clean STO is measured to be 3.9 Å, which means single termination.

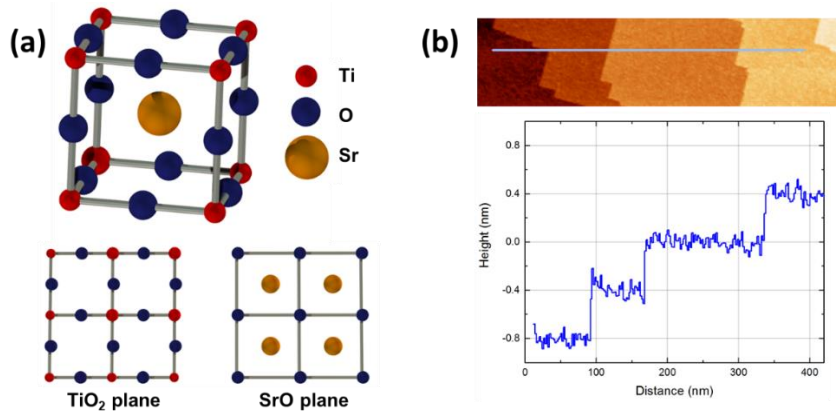

Figure 4.4: Termination of $SrTiO_3$(100): (a)Structure of $SrTiO_3$ and (b) line profile of clean $SrTiO_3$ (100)

Target

The target used for growth was electron-doped $Ba(Fe_{1-x}Co_x)_2As_2$ with cobalt concentration x = 0.08 polycrystalline pellets with diameter 1/2". The pellet was prepared by conventional solid state reaction using Fe_2As, BaAs and Co_2As as precursors. A detailed recipe refers to H. Hosono *et al* [111]. The crystallinity and superconductivity of the pellets were confirmed by X-ray diffraction and magnetic susceptibility measurements, respectively.

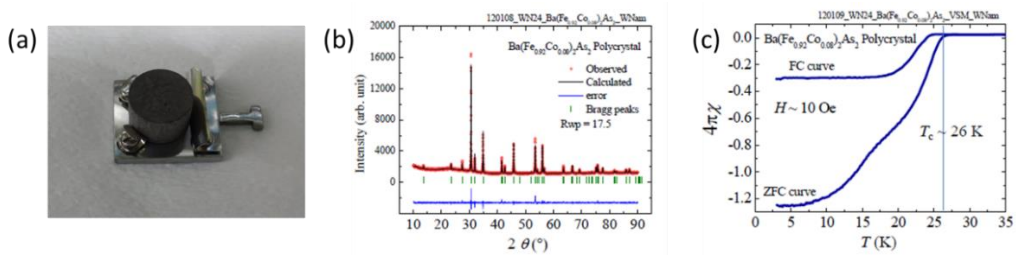

Figure 4.5: Target preparation: (a) Picture of the 1/2 "diameter pellet used in the experiment. (b) The XRD results show that the target is polycrystalline. (c) Superconducting transition was confirmed by magnetic susceptibility measurement.

The measurement of the pellet was made by Woohyun Nam in group of Prof. Kee hoon Kim at Seoul National University. The target was positioned at a distance of 40 mm from the sample. In this experiment, the target was rotated with 10 RPM and the laser ablation repetition rate was set to 10 Hz.

Mass (g)	Diameter (mm)	Height (mm)	Volume (cm^3)	ρ (g/cm^3)	ρ_{cal} (g/cm^3)
4.470	11.67	7.49	0.801	5.58	6.51

Table 4.1: Density of the target: (ρ/ρ_{cal}~86%)

Temperature Optimization

Growth conditions must be optimized to obtain epitaxial growth of $Ba(Fe_{1-x}Co_x)_2As_2$. Surface morphology studies on growth temperature have been rarely studied compared to superconducting properties and structural studies, and have not been studied with STM. Using the growth conditions described above, growth was performed at deposition rate of 4.8 ML in 1200 pulse. *In-situ* imaging with STM was conducted to find the growth

temperature window while varying the growth temperature at 650, 675, 700, and 750 °C. The following results are the RHEED pattern with e-beam along with [100] direction of STO and the corresponding STM image of 4.8ML films grown using 10 Hz, 100 mJ (corresponding fluence is 2.5 J/cm^2) laser conditions.

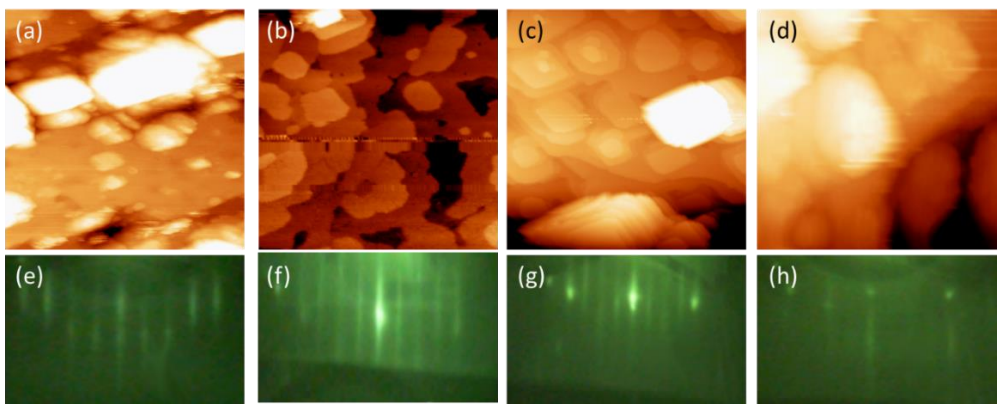

Figure 4.6: Optimization of growth temperature: STM images of $Ba(Fe_{1-x}Co_x)_2As_2$ 10 ML films grown at different substrate temperature with size of 255 nm×255 nm and corresponding RHEED patterns. (a) 650 °C, (b) 675 °C, (c) 700 °C, and (d) 750 °C.

Sharp RHEED streaks were observed at substrate temperatures between 650 °C and 700 °C. This pattern shows epitaxial thin film growth. The elongated streak on the 0-th Laue zone is due to the high density of step and can be seen in the corresponding STM image. Despite the absence of large changes in the RHEED pattern at temperatures between 650 °C and 700 °C, there is a difference in the surface scanned by STM. At 650 °C, the rectangular islands grow, but the steps are not clearly separated. At 675 °C, rectangular islands with flat terraces grown, but there are some irregular islands too. At 700 °C, the square shaped island is distributed with clearly visible steps. The average size of the terraces at this temperature is ~ 20 nm. In this temperature window, the higher the temperature, the smaller the size of the terrace and the higher the island density. Due to the

temperature-dependent initial nucleation density, it is deduced that the islands grow from the nucleus. At temperatures above 750 °C, RHEED streaks are vague, indicating that crystallinity is poor, and rough surfaces can be identified by STM. In this study, T_S was optimized at 700±25 °C.

Fluence Optimization

Laser fluence is important for stoichiometric deposition. Too weak laser luminescence cannot perform stoichiometric removal of the target material, and too strong fluence can cause droplet formation problems that often occur in PLD. Since fluence and deposition rate are trade-off, laser parameter tuning is indispensable for research. In this case, the RHEED pattern beam along with [100] direction of STO was observed and the substrate temperature at 700 °C and depositing 4.8 ML of $Ba(Fe_{1-x}Co_x)_2As_2$.

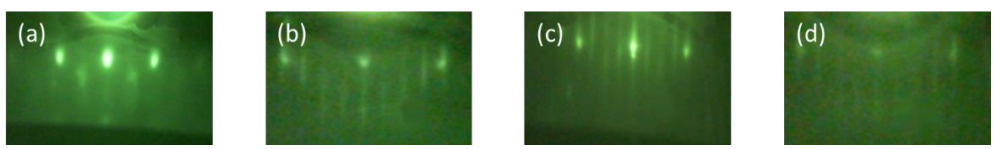

Figure 4.7: RHEED pattern of pulse energy optimization: The growth were performed at different pulse energy 40, 60, 100 and 140 mJ and the corresponding fluences were 1, 1.5, 2.5 and 3.5 J/cm^2, respectively.

Laser ablation was performed at pulse energy 40, 60, 100, and 140 mJ, and the corresponding fluences were 1, 1.5 ,2.5 and 3.5 J/cm^2, respectively. At pulse energy 40 mJ, 3D RHEED peaks are noticeable due to off-stoichiometry cluster formation. At 60 mJ and 140 mJ, surface is partially crystalized but the intensity of streaks is weak. Therefore, fluence was set to 100mJ.

4.4 Surface Studies of $Ba(Fe_{1-x}Co_x)_2As_2$ film on $SrTiO_3(100)$

4.4.1 Surface Reconstruction

In PLD grown thin film of $Ba(Fe_{1-x}Co_x)_2As_2$, $2\sqrt{2} \times 2\sqrt{2}$ R45° surface reconstruction was unexpectedly observed in STM, LEED, and RHEED. This is a different surface reconstruction from $\sqrt{2} \times \sqrt{2}$ or 2×1, which was seen on the low-temperature cleaved $BaFe_2As_2$ cleaved surface [85,87]. Figure 4.8 (a) shows that the protruding blobs in the STM image are regularly distributed in a square grid with a spacing of 1.12 nm. Half-filled Ba surface is energetically more stable and satisfies charge neutrality than full covered Ba over-layer. So, this blobs are considered to be a cluster of four Ba atoms rather than one Ba atom, which is consistent with energy and charge criterion. This feature can also be seen in that the cluster appears as a ring shape under certain imaging conditions. With this topography as a hint, the location of the four barium in the unit of the reconstruction cell is discussed. Energy stability is calculated by density functional theory calculation for the possible configurations, and as a result, the configuration of four barium atoms shifted to the center of blobs in the $2\sqrt{2} \times 2\sqrt{2}$ R45° is most stable, as shown in Figure 4.8 (b).

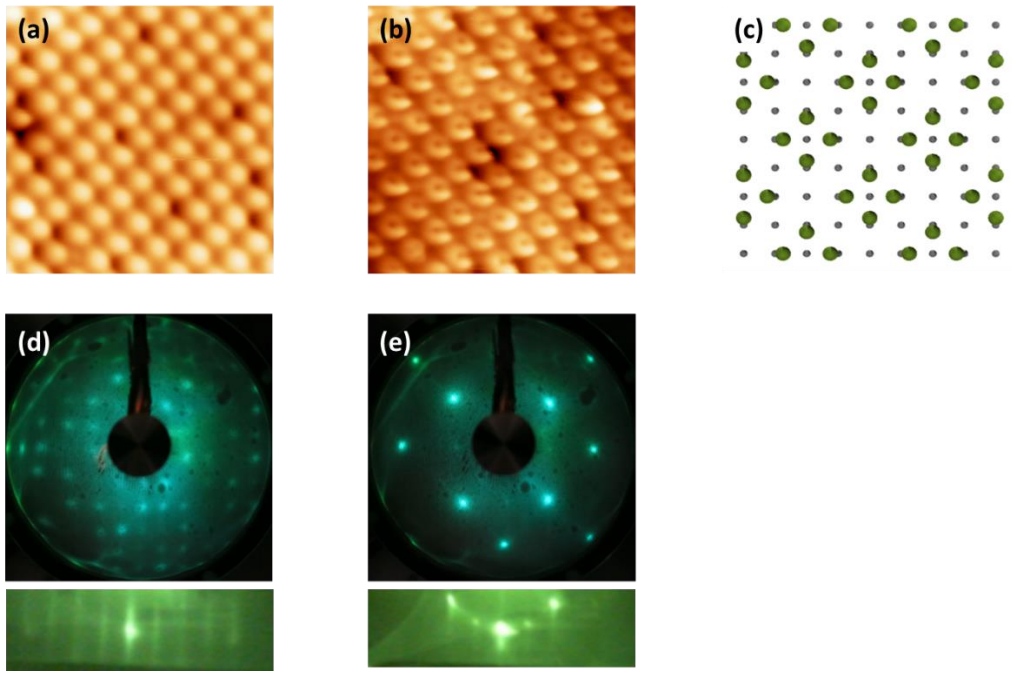

Figure 4.8: $2\sqrt{2} \times 2\sqrt{2}$ R45° Surface reconstruction: STM images of 10.5 nm×10.5 nm obtained at different bias. (a) -500 mV and (b) -200mV, (c) Schematic configuration of surface reconstruction, LEED pattern obtained at 70 eV and RHEED pattern obtained at 12 keV of (d) as grown $Ba(Fe_{1-x}Co_x)_2As_2$ and (e) clean $SrTiO_3(100)$.

In Figure 4.8 (d), (e), the LEED results show that more peaks are found inside the 1×1 peaks of STO compared to before. These additional spots are spanned by reciprocal lattice basis $\frac{\overrightarrow{b_1}+\overrightarrow{b_2}}{4}$, $\frac{\overrightarrow{b_1}-\overrightarrow{b_2}}{4}$. That is, $2\sqrt{2} \times 2\sqrt{2}$ R45° surface reconstruction. When the RHEED beam along with [100] direction of STO, it can be seen that $2\sqrt{2} \times 2\sqrt{2}$ R45° streaks are located at same position of 2×2 surface reconstruction of STO. In the reciprocal lattice space, $2\sqrt{2} \times 2\sqrt{2}$ R45° reconstruction streaks are in the same position of the 2×2 STO reconstruction because it bisects nearest 1×1 and divides the

diagonal 1×1 into quadrants. Since the electron diffraction results reflect the structure by scatter, the surface reconstruction measured by STM is not an artificial effect.

4.4.2 Surface Features

PLD grown $Ba(Fe_{1-x}Co_x)_2As_2$ has unique surface features. These features that are not seen in the cleaved bulk are the phenomena governed by the growth kinetics and thermodynamic laws during film growth process.

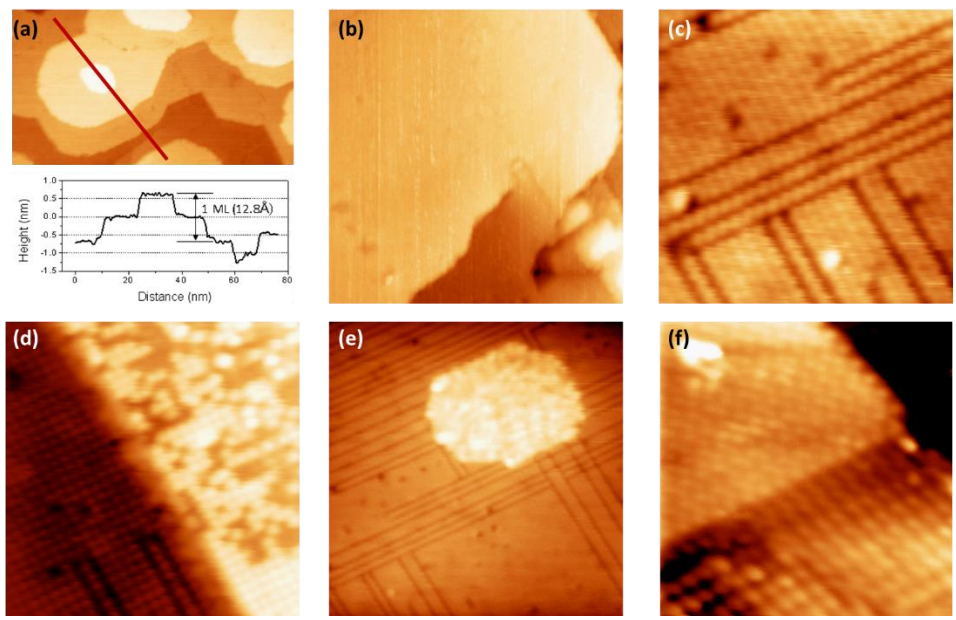

Figure 4.9: Surface features of as-grown $Ba(Fe_{1-x}Co_x)_2As_2$ film: (a) Half unit cell step, (b) Screw dislocation, (c) Ordered missing rows, (d) Missing atoms, (e) Excess Ba cluster, (f) Exposed area with step height less than half unit cell.

Figure 4.9 (a) shows the STM results of the 12 ML grown $Ba(Fe_{1-x}Co_x)_2As_2$ film and the height profile of the line cut. In all samples grown more than 4 ML, the step height was

integer multiple of 6.4 Å, which is half of the unit cell height. This means that the growth occurs in units of blocks corresponding to half of the unit cell, which also support that the top most layer is a Barium layer. Figure (b) is a screw dislocation often seen in the crystal growth and (c) is ordered missing rows. The spacing of these rows is 16.8 Å or 22.4 Å. This is due to the slipped geometry between $2\sqrt{2} \times 2\sqrt{2}$ R45° ordered domains. Rarely, in the area where the uniformity of the Ba content is broken, a deficient region may appear as shown in (d), and an excess region may appear as shown in (e). The top layer is Ba layer because the low surface energy plane is exposed in the grown sample. Therefore, very rarely, a surface with a step height less than half unit cell is exposed as shown in (f).

4.5 Electronic Structures of $Ba(Fe_{1-x}Co_x)_2As_2$ on $SrTiO_3$

The thin film grown by PLD was measured in other STM system, which has good temperature stability dewar with operation temperature of 4.3 K with help of the vacuum transfer chamber described in the previous chapter. The deposition conditions are the same as in the previous section, and the measurement was performed on 10 ML films at 4.3 K.

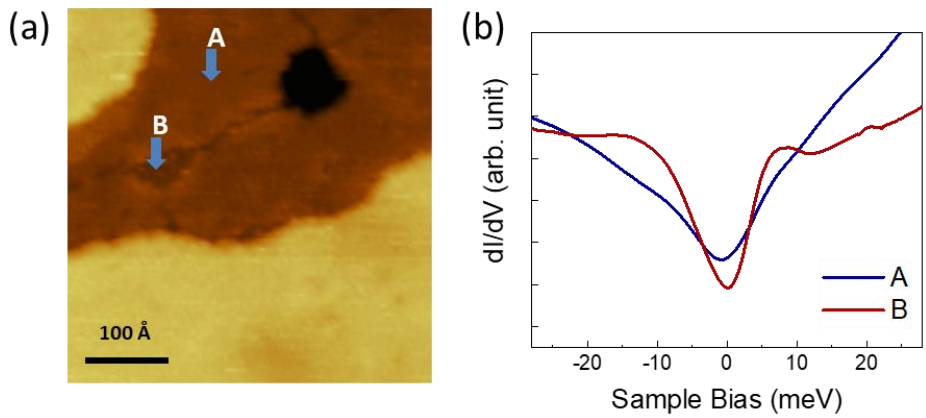

Figure 4.10: Ba Layer screening of superconducting gap: (a) Topographic image of 10 ML $Ba(Fe_{1-x}Co_x)_2As_2$ on $SrTiO_3(100)$. (b) dI/dV spectrum obtained at the indicated regions. A : on Ba site, B: depressed region.

As can be seen from the Figure 4.10, excellent sample quality is preserved after *in-vacuo* sample transfer. $2\sqrt{2} \times 2\sqrt{2}$ R45° surface is observed in most areas. However, occasionally, surface with step height less than half unit cell appears. Figure 4.10 (b) shows the dI/dV spectrum on top layer A and depressed layer B. The tunneling spectrum on A region has V Shape gap similar to the result from the cleave sample and the size of gap Δ is about 6 meV. On the other hand, on the B region, the coherence peak and the gap are more apparent. This result shows that the superconducting gap of Ba-122 is screened so that the direct probing of superconducting layer is prevented by barium layer.

Quasi particle interference is a technique of mapping the local density of state spatially and obtaining the result by fast fourier transform [89,102]. This result gives an interference pattern of the momentum caused by the transition of the quasiparticle. Thus, the symmetry of the bulk superconducting order parameter can be measured. This method can be applied to measure the charge order of surface. In systems such as $Ba(Fe_{1-x}Co_x)_2As_2$, where the

screen of the surface layer is strong, the fourier transform of the image makes it possible to directly probe the charge order.

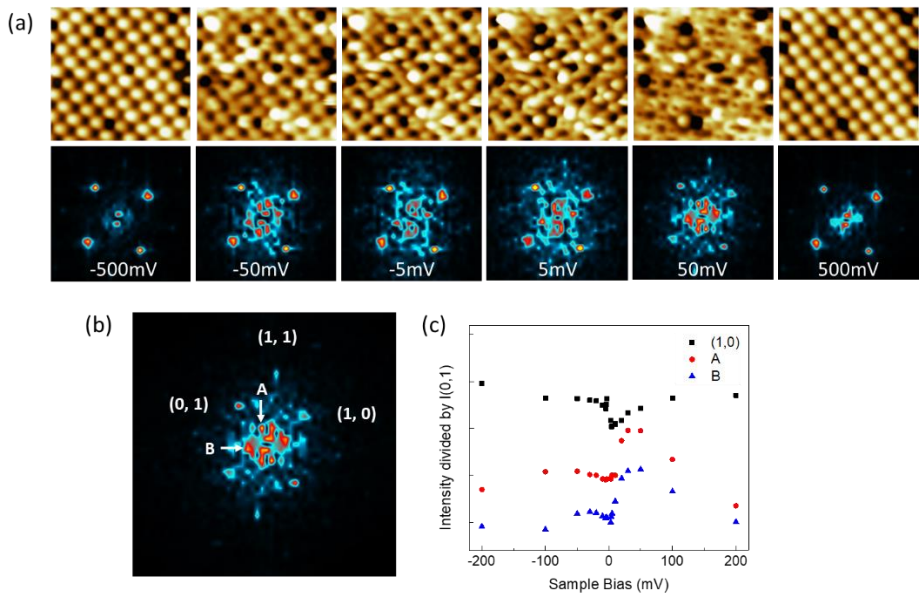

Figure 4.11: Charge modulation appearance at the vicinity of the superconducting gap: (a) Topographic images with size 10 nm × 10 nm at different bias and corresponding FFT images. (b) Close up view of FFT images obtained at 50 mV. (c) Intensity plot as varying bias.

$Ba(Fe_{1-x}Co_x)_2As_2$ surface is measured at different voltages in order to observe the electronic structure corresponding to the specific energy in real space by bias dependent imaging. Figure 4.11 show the bias-dependent surface topographic images and corresponding fast fourier transformation (FFT) images. When the voltage is high, it looks like a regular checkerboard, but when the voltage goes near the superconducting gap, the regular pattern is blurred and the blobs change to ring shape. This feature can be seen from the result of tracing the intensity of several peaks in the FFT image with different energy. Where (1, 0) represents $2\sqrt{2} \times 2\sqrt{2}$ R45° order, strong outside the superconducting gap,

and weak near the gap. However, as the voltage approaches the superconducting gap, the other peaks A and B appear pronounced. These peaks are A $(\frac{1}{6},\frac{1}{3})$ and B $(-\frac{1}{2.5},\frac{1}{3})$, they correspond to the charge order of the long wave length. This observation confirmed that the charge modulation is at the vicinity of the superconducting gap.

4.6 Transport Measurement

The most direct way to confirm the superconductivity of a material is to make sure that the resistivity drops abruptly to zero when the temperature drops below transition temperature. Therefore, in this study, superconductivity was confirmed by transport measurement on 100 ML of $Ba(Fe_{1-x}Co_x)_2As_2$ grown by PLD, that is, resistivity was measured as function of temperature change.

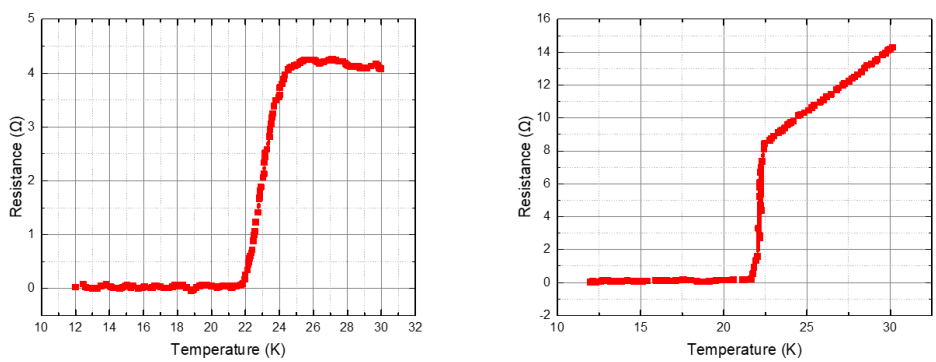

Figure 4.12: Transport measurement of 100 ML $BaFe_2As_2$ films: *in-situ* (left), *ex-situ* (right)

Ex-situ measurement, undoped $SrTiO_3$ (100) was used as a substrate. The wet treatment was the same as the conventional Nb doped STO substrate, but the PBN heater was used instead of the direct DC anneal. Thickness of the film was 100 ML (128 nm), and the

deposition conditions except for the substrate were the same. The epitaxial growth was confirmed by RHEED pattern of as-grown sample. The mechanical contacts were made with 4 etched tungsten tips in argon filled glove box. Superconducting transition were observed with T_{onset} = 22 K and T_{zero}=21 K. *In-situ* transport measurements were performed on the other STM system designed to mount mircro 4-point probe on an STM scanner. 100 ML of $Ba(Fe_{1-x}Co_x)_2As_2$ films were deposited with optimized conditions and then transferred to the transport-STM using the vacuum transfer chamber. Superconducting transition was observed at T_{onset}= 23.96 K and T_{zero}= 22 K and superconductivity was confirmed.

4.7 Initial Stage of $Ba(Fe_{1-x}Co_x)_2As_2$ Growth

$Ba(Fe_{1-x}Co_x)_2As_2$ thin film grows c-axis epitaxial when it grows more than 4 ML, and its structural properties are revealed by LEED, RHEED and STM. Then, naturally, you can think about the possibilities for ultra-thin films or 2D superconductors. The RHEED evolution over the film deposition under optimized conditions can be seen in Figure 4.10.

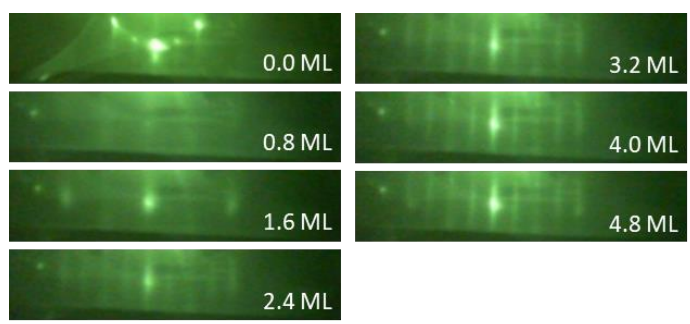

Figure 4.13: Time evolution of RHEED pattern of $Ba(Fe_{1-x}Co_x)_2As_2$ films

The absence of an abrupt interface in the sub-monolayer regime can be seen by the diffuse peak and cluster formation by RHEED. At this time, due to the clusters formation the initial stage of deposition, the first three layer form island growth mode instead of ideal layer by layer growth. As this island ledge grew and merged, a flat terrace is formed. and the stresses generated during this process is observed in form of the screw / edge dislocation seen in the previous section.

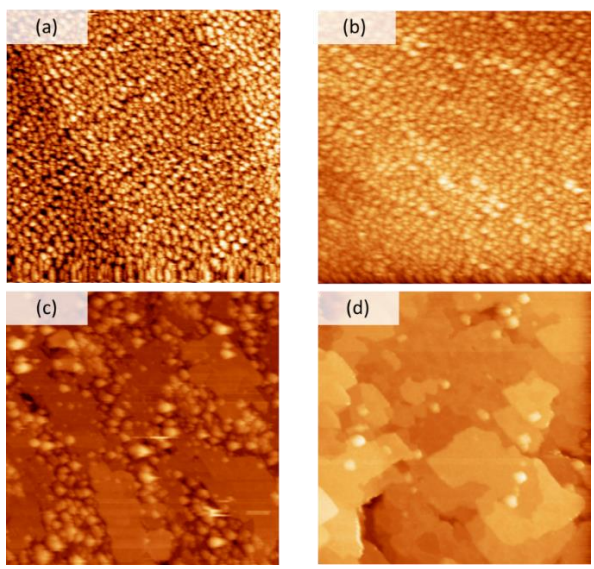

Figure 4.14: Topography of initial growth stages of $Ba(Fe_{1-x}Co_x)_2As_2$ films : (a) 0.5 ML, (b) 1.5 ML, (c) 3 ML, (d) 4.5 ML. Images obtained with size 210 nm × 210nm.

As shown in Figure 4.14, there is no flat ordered area up to 1.5 ML, only clusters are formed. This can be seen in 3D peaks in RHEED pattern in Figure 4.10. This suggests that the kinetic collision on substrate due to PLD process may interfere with the creation of the abrupt interface. At 3 ML, the ordered domain areas emerge and the domain has $2\sqrt{2} \times$

$2\sqrt{2}$ R45° surface recombination. And as growth progresses, the islands merge leaving the line defects.

Chapter 5. Pulsed Laser Deposition Growth of LiFeAs

5.1 Introduction

Immediately after the synthesis of the first Fe-based high temperature superconductor (HTS) [30,31], LiFeAs, belonging to "111"-family, in which Li interlace FeAs layers, was synthesized and studied [43,112]. LiFeAs has transition temperature with 18 K and has anisotropic full gap structures on multiband [78,79,113,114]. LiFeAs has unusual properties in several ways with other Fe-based HTS. First, LiFeAs is one of few Fe-based HTS that are stoichiometric intrinsic superconductors at ambient pressure and without doping. Compared to other stoichiometric superconductors KFe_2As_2 (T_C = 3 K) [42] or LaFePO (Tc = 5.6 K), LiFeAs has relatively high transition temperature of 18 K than others [43]. And unlike other Fe-based HTS, this material does not undergo tetragonal to orthorhombic structural phase transitions under pressure or temperature [115,116]. In other Fe-based HTS like "122" and "1111" family, nesting occurs through the anti-ferromagnetism wave vector [117,118], but LiFeAs has no nesting properties and no static spin ordering, suspected to be origin of superconductivity in Fe-based HTS [119]. And still there are debating on order parameter symmetry that previous results do not directly support any model of s, d, s++, s+- wave. Therefore, LiFeAs is an unusual iron-based superconductor with many fields to be studied.

Extensive studies on LiFeAs were done with bulk grown sample. Many iron-based HTS have the disadvantage of not being able to cleave well [79]. However, LiFeAs is known to exhibit Li-terminated neutral cleave plane without surface reconstruction and shows bulk like properties due to absence of surface state [120]. Thus, previous studies on the cleaved surface of LiFeAs have been done using surface sensitive probing tools such as ARPES [114,119] and STM [77–79,81]. However, film growth has not been reported so

far except for one MBE grown film [121]. In this study, we discuss the growth mechanism of LiFeAs film grown by PLD. By adjusting the growth parameters, surface morphology and structural changes are analyzed using surface inspection tools STM, RHEED and LEED.

5.2 Structural Properties of LiFeAs

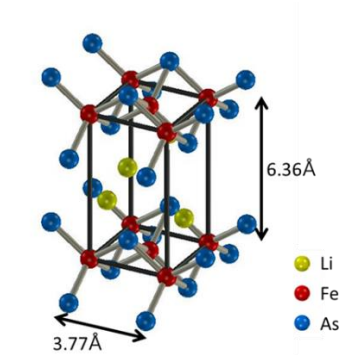

Figure 5.1: Crystal structure of LiFeAs

The crystal structure of LiFeAs is tetragonal PbFCl type (P4/nmm) which is shown at Figure 5.1. According to previous X-ray diffraction studies, the lattice constants for each direction are a = b = 3.77 Å and c = 6.36 Å [43,112,122]. As in the structure of the FeAs layer in a typical iron-based superconductor, arsenic atoms are alternately located above and below at the center of Fe square net. That is, there is an iron square layer between two square As layers, which is as large as $\sqrt{2}$ times of Fe-Fe distance (2.68 Å) and rotated by 45°. The FeAs layers do not have slipped stacking as in the case of 122 compound, but rather a parallel stacking configuration like “11” and “1111” family. There are lithium double layers between the FeAs layers. Structural studies of thin film LiFeAs are not as

diverse as in bulk. No surface reconstruction was reported. And lattice relaxation was studied, i.e., thickness dependence of lattice parameter and superconducting gap was examined [121].

5.3 Growth Conditions of LiFeAs on $SrTiO_3$(100)

Target

In this study, LiFeAs single crystal was used as a target. The size of the LiFeAs piece is about to 8 mm × 5 mm × 3 mm, and the piece with a flat top was selected considering plume formation. The following figure shows that LiFeAs single crystal piece is attached to the target holder. Since the size of the target is smaller than that of a commercially available target and the surface is uneven, the plume generated when the laser strikes the target should be adjusted to face the substrate.

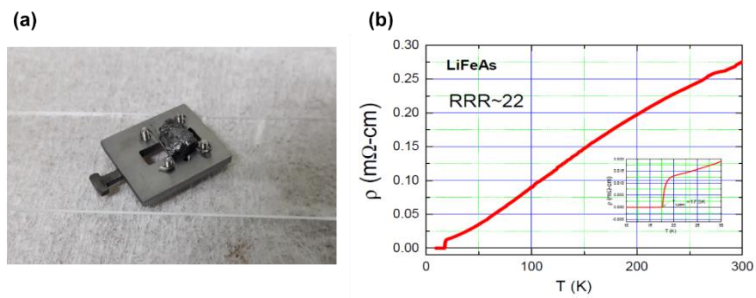

Figure 5.2: LiFeAs Target: (a) Picture of LiFeAs single crystal target attached to the target holder. (b) Measurement of the resistivity of target as function of temperature. Superconducting transition occurs at 17.5 K.

The targets used here were synthesized by Professor Yong Seung Kwon's group in DGIST. The electrical resistivity measurement of the target is as follows and the measured transition temperature is 17.5K.

Temperature Optimization

Thin film growth of HTS exhibits different superconducting performance depending on growth conditions such as doping and growth temperature, and these researches have been extensively studied because they can be applied to industrial applications. In order to achieve stoichiometric epitaxial PLD growth of LiFeAs thin films which is not reported yet, surface analysis was performed at different temperatures to find the optimal growth temperature window. In this study, the pulse energy was set to 150 mJ and the corresponding fluence was 3.75 J/cm^2. The distance between the target and the substrate was adjusted to 40 mm and laser ablation repetition was 1 Hz. The reason for choosing slower repetition rate compared to previous studies is that it is difficult to rotate the target due to the small, curved target surface. In order to compare growth morphology, 300 shots were deposited, and the amount of deposition corresponds to 3 QL. Using the above conditions, depositions were performed at 400, 450, 500 and 550 °C. The following figure 5.3 shows 210 nm × 210 nm STM images and corresponding LEED (inset) and RHEED pattern grown at different temperature.

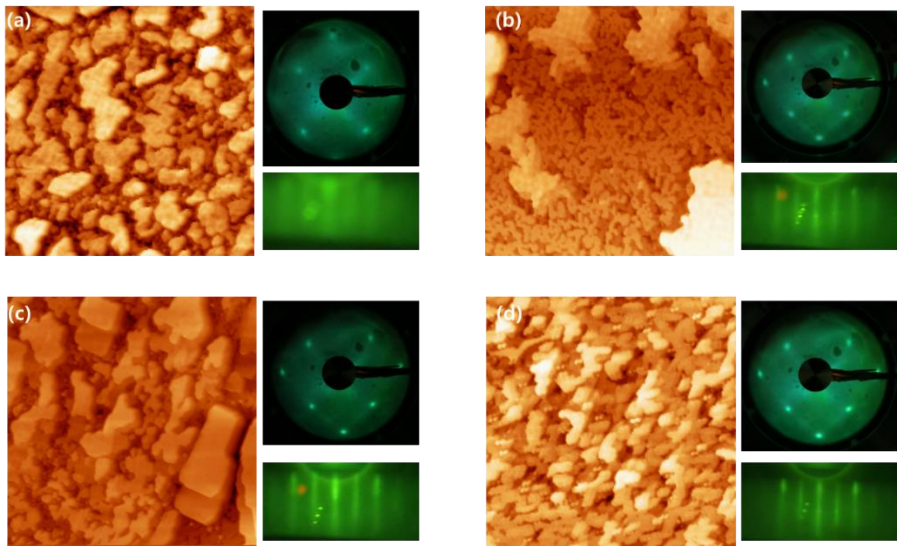

Figure 5.3: As-grown LiFeAs films grown at different temperature: STM images (210 nm × 210 nm), LEED measured at 40 eV and RHEED with incidence e-beam along with [100] orientation. The films grown at (a) 400 °C, (b) 450 °C, (c) 500 °C, and (d) 550 °C.

At all growth temperatures, LEED shows LiFeAs 1×1 structure without any surface reconstruction. RHEED patterns show distinct 1×1 structure between 450 and 550 °C, but at 400 °C, faint streak meaning poor crystallinity appears. After deposition of 2 QL of wetting layer at 450 ~ 550 °C, island growth mode is followed. At 450 °C, lateral growth of islands of 50 nm or more in size with a flat top surface is seen. At 500 and 550 °C, the islands grow but their size is small and grow like cluster formation.

Fluence Optimization

In order to achieve good quality stoichiometric deposition, it is necessary to adjust the proper fluence. Surface morphology was measured with the variation of fluence under the following conditions. The target substrate distance of 40 mm and the optimized temperature of 500 °C, and the repetition rate of 1 Hz. The pulse energies are 100, 125 and

150 mJ, respectively, and the corresponding fluences are 2.5, 3.125 and 3.75 J/cm2, respectively.

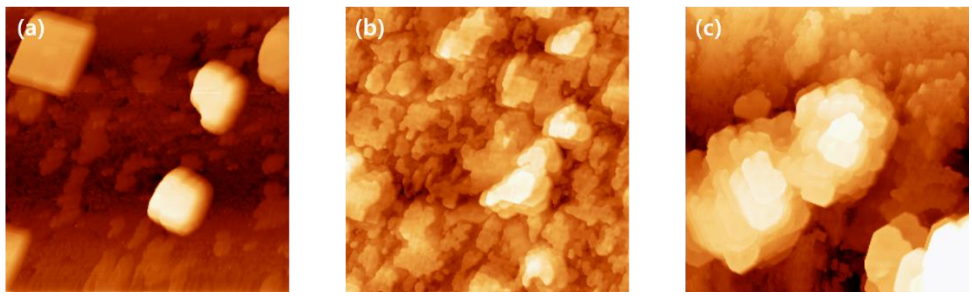

Figure 5.4: As-grown LiFeAs films grown at different pulse energy: STM images of 340nm×340nm images and corresponding RHEED patterns. Films grown at 500 °C, 1 Hz and 600 pulses of deposition. (a) 100 mJ, (b) 125 mJ, and (c) 150 mJ.

Growth Conditions

As in the previous chapter, $SrTiO_3$ (100) was used as a substrate. The same wet etching and annealing treatments were used for single TiO_2 termination. Laser ablation repetition rate and sample target distance were kept as before.

5.4 Surface Studies of LiFeAs on $SrTiO_3$(100)

Growth mode

The initial growth of films follows the Stranski-Krastanov mode, and the island forms on the 2 QL of wetting layer. In the growth process, clusters are merging into oriented attachment mechanisms.

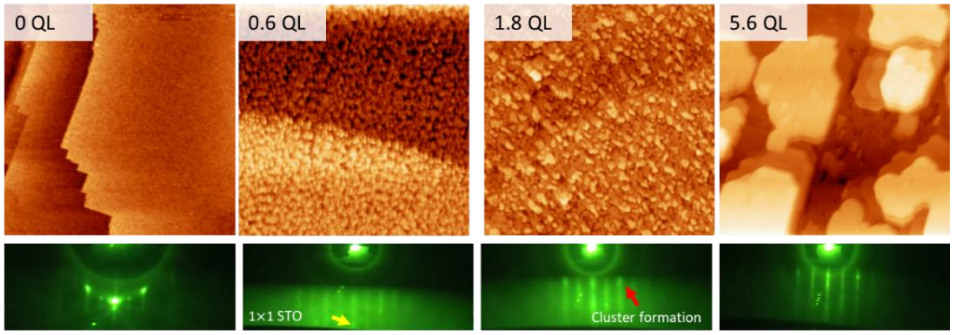

Figure 5.5: Surface morphology evolution as thickness varies. Images are obtained at 340 nm × 340 nm size. (a) Before growth, (b) 0.6 QL, (c) 1.8 QL and (d) 5.6 QL deposited.

The wetting layer has a unique shape. This layer has orthogonal missing rows. The wetting layer also has a stepped structure with a height of 6.4 Å, which is equal to the height of the LiFeAs unit cell. And once the wetting layer has covered the surface, the 3D-islands start to grow to relieve the stress from substrate, and their heights vary widely. There are Moiré patterns on the flat top of the islands. This pattern is not regular but depends on the shape of the island, and the average spacing is ~ 38 Å. The corrugation of this pattern in z direction is ~ 1 Å for 2 QL height island and smaller for higher island.

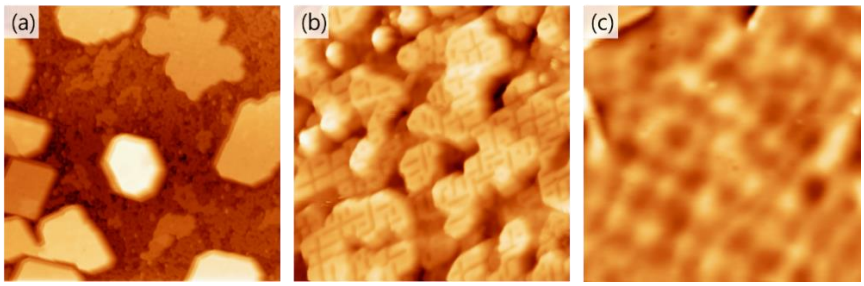

Figure 5.6: Surface features of as-grown LiFeAs film. (a) Islands grown on 2 QL of wetting layers (340 nm × 340 nm), (b) Magnified view of wetting layers (85 nm × 85 nm) and (c) Moiré pattern on flat top of island (51 nm × 51 nm).

Determination of lattice constant

LiFeAs thin film was deposited onto $SrTiO_3$ (100) under the conditions optimized above. In order to understand the properties of the deposited film, the lattice constant and its structure were confirmed. As shown in Figure 5.6, the LiFeAs film has square atomic arrangement with step height of integer multiple of 6.4 Å, which corresponds to the unit cell height of LiFeAs. And on the island of 6 QL height, the atomic resolution image yields an in-plane lattice parameter of ~ 3.75 Å. This is close to the lattice constant of the bulk of the stress released and also consistency with the value of previous studies in MBE grown film. A comparison of the lateral spacing of RHEED streaks also confirms that the in-plane lattice constant is ~3.80 Å when LiFeAs were deposited at an amount corresponding to 10 QL.

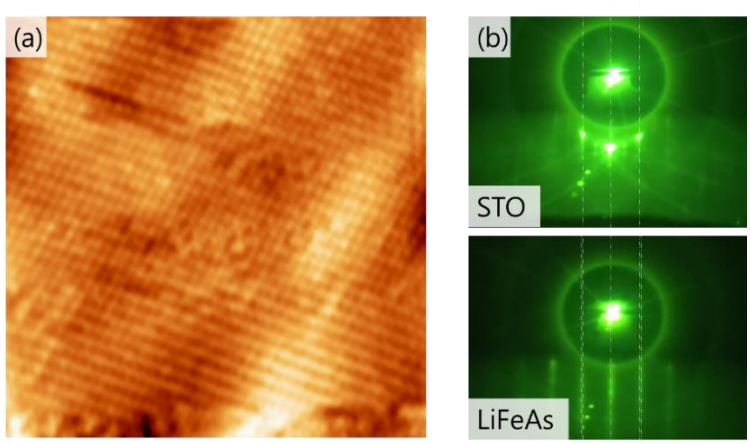

Figure 5.7: Determination of lattice constant: (a) Topography of island flat top obtained at 0.2 V, 200 pA, size of 13.9 nm× 13.9 nm, and (b) Change in lateral spacing of RHEED streaks.

5.5 Growth interruption

Since the growth of LiFeAs using typical PLD technique proceeds by 3D island growth, it is difficult to conduct experiments using STM. This is because there is a risk that the tip may crush to the island where the z-feedback of the STM is hard to work, and QPI require the large flat area of field of view which Nyquist sampling theorem is secured. In order to obtain layer by layer mode, the growth of the previous layer must be completed before the top most layer starts to nucleate. Otherwise, growth will occur in multi-layer growth manner. In this study, growth interruption technique is applied to achieve close to layer by layer growth mode by increasing interlayer mass transport. This technique is realized by repeating cycles of 1 QL depositing and then having subsequent relaxation time for recrystallization.

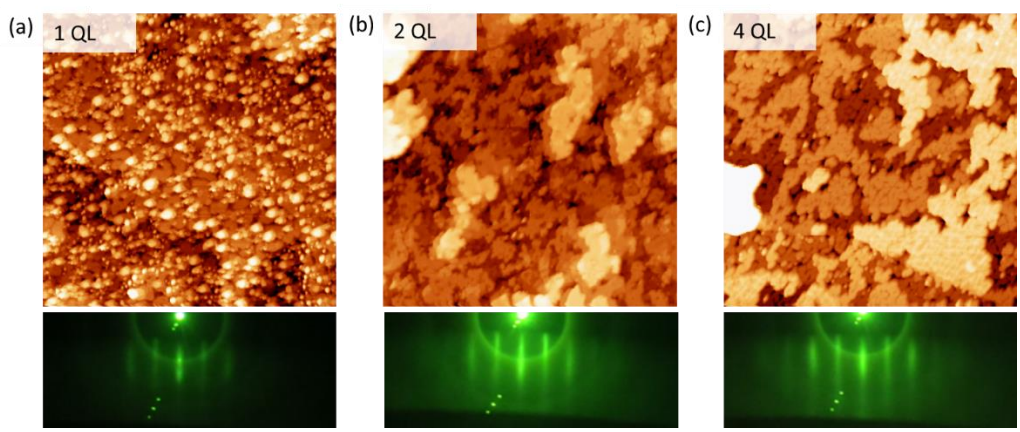

Figure 5.8: Sequential images during interruptive growth. Images are obtained at 340 nm × 340 nm size. (a) 1 QL, (b) 2 QL and (d) 4 QL deposited.

Figure 5.8 shows the results obtained by the growth interruption technique. The interval time between each 1 QL is 30 minutes, which is longer than the characteristic relaxation time ~ 0.5 sec. As shown in the figure, island growth was suppressed. And it can be

confirmed that multi-level growth is also suppressed compared to the previous conditions. The surface has a large terrace size of ~ 100 nm instead of island formation when the thickness is 4 QL. With help of growth interruption technique, an improved surface quality can be obtained compared to the standard PLD method, and the layer by layer mode growth suitable for the STM experiment could be achieved.

Chapter 6. Conclusion

In this study, the author constructed STM combined with Laser-MBE (MBE / PLD) system to measure the epitaxial thin film of high-temperature superconductor. Using this system, the author performed epitaxial films growth of two kinds of iron - based superconductor Co doped $BaFe_2As_2$ and LiFeAs. Growth conditions and STM analysis of each material were performed.

Co-doped $BaFe_2As_2$ thin film was measured witht STM for the first time in this study. Under optimized deposition conditions, this film showed unique $2\sqrt{2} \times 2\sqrt{2}$ R45° surface reconstruction which is different from the cleaved bulk. And several surface features that have not been reported have been observed. the superconducting gap screened by the Ba layer were observed. And the charge modulation near the superconducting gap was measured. The superconductivity was confirmed by measurement of superconducting gap and *ex / in-situ* transport measurement.

The thin film LiFeAs was grown by PLD technique for the first time. Optimization of growth condition was presented. The initial growth of LiFeAs films follows the Stranski-Krastanov mode, and the island forms on the 2 QL of wetting layer. Growth was interrupted for the larger terrace size. Using this pulsed laser interval growth technique, a good quality LiFeAs film could be grown.

Bibliography

[1] B. D. Josephson, Phys. Lett. **1**, 251 (1962).

[2] J. M. Kosterlitz and D. J. Thouless, J. Phys. C Solid State Phys. **6**, 1181 (1973).

[3] M. P. A. Fisher, Phys. Rev. Lett. **65**, 923 (1990).

[4] Y. Guo, Y.-F. Zhang, X.-Y. Bao, T.-Z. Han, Z. Tang, L.-X. Zhang, W.-G. Zhu, E. G. Wang, Q. Niu, Z. Q. Qiu, J.-F. Jia, Z.-X. Zhao, and Q.-K. Xue, Science **306**, 1915 (2004).

[5] Y.-F. Zhang, J.-F. Jia, Z. Tang, T.-Z. Han, X.-C. Ma, and Q.-K. Xue, Surf. Sci. **596**, L331 (2005).

[6] A. T. Bollinger and I. Božović, Supercond. Sci. Technol. **29**, 103001 (2016).

[7] W. Qing-Yan, L. Zhi, Z. Wen-Hao, Z. Zuo-Cheng, Z. Jin-Song, L. Wei, D. Hao, O. Yun-Bo, Deng Peng, C. Kai, W. Jing, S. Can-Li, H. Ke, J. Jin-Feng, J. Shuai-Hua, W. Ya-Yu, W. Li-Li, C. Xi, Ma Xu-Cun, and X. Qi-Kun, Chin. Phys. Lett. **29**, 037402 (2012).

[8] M. M. Ugeda, A. J. Bradley, Y. Zhang, S. Onishi, Y. Chen, W. Ruan, C. Ojeda-Aristizabal, H. Ryu, M. T. Edmonds, H.-Z. Tsai, A. Riss, S.-K. Mo, D. Lee, A. Zettl, Z. Hussain, Z.-X. Shen, and M. F. Crommie, Nat. Phys. **12**, 92 (2016).

[9] S. Lee, J. Jiang, Y. Zhang, C. W. Bark, J. D. Weiss, C. Tarantini, C. T. Nelson, H. W. Jang, C. M. Folkman, S. H. Baek, A. Polyanskii, D. Abraimov, A. Yamamoto, J. W. Park, X. Q. Pan, E. E. Hellstrom, D. C. Larbalestier, and C. B. Eom, Nat. Mater. **9**, 397 (2010).

[10] X. Xi, Z. Wang, W. Zhao, J.-H. Park, K. T. Law, H. Berger, L. Forró, J. Shan, and K. F. Mak, Nat. Phys. **12**, 139 (2016).

[11] D. B. Haviland, Y. Liu, and A. M. Goldman, Phys. Rev. Lett. **62**, 2180 (1989).

[12] A. Yazdani and A. Kapitulnik, Phys. Rev. Lett. **74**, 3037 (1995).

[13] H. K. Onnes, Commun Phys Lab Univ Leiden **120b**, **122b**, **124c**, (1911).

[14] P. Drude, Ann. Phys. **306**, 566 (n.d.).

[15] W. Meissner and R. Ochsenfeld, Naturwissenschaften **21**, 787 (1933).

[16] F. London and H. London, Proc R Soc Lond A **149**, 71 (1935).

[17] F. London, *"Superfluids"* (Wiley, New York, 1950).

[18] A. B. Pippard and W. L. Bragg, Proc R Soc Lond A **216**, 547 (1953).

[19] T. E. Faber and A. B. Pippard, Proc R Soc Lond A **231**, 336 (1955).

[20] J. Bardeen, L. N. Cooper, and J. R. Schrieffer, Phys. Rev. **108**, 1175 (1957).

[21] E. Maxwell, Phys. Rev. **78**, 477 (1950).

[22] G. M. Eliashberg, Sov Phys - JETP Engl Transl U. S. **11:3**, (1960).

[23] V. GINZBURG, Zh Eksper Teor Fiz **20**, 1064 (1950).

[24] A. A. ABRIKOSOV, Sov Phys JETP **5**, 1174 (1957).

[25] H. F. Hess, R. B. Robinson, R. C. Dynes, J. M. Valles, and J. V. Waszczak, Phys. Rev. Lett. **62**, 214 (1989).

[26] L. P. Gor'kov, Zh Eksper Teor Fiz **9**, 1364 (1959).

[27] G. F. Hardy and J. K. Hulm, Phys. Rev. **89**, 884 (1953).

[28] J. G. Bednorz and K. A. Müller, Z. Für Phys. B Condens. Matter **64**, 189 (1986).

[29] M. K. Wu, J. R. Ashburn, C. J. Torng, P. H. Hor, R. L. Meng, L. Gao, Z. J. Huang, Y. Q. Wang, and C. W. Chu, Phys. Rev. Lett. **58**, 908 (1987).

[30] Y. Kamihara, T. Watanabe, M. Hirano, and H. Hosono, J. Am. Chem. Soc. **130**, 3296 (2008).

[31] Y. Kamihara, H. Hiramatsu, M. Hirano, R. Kawamura, H. Yanagi, T. Kamiya, and H. Hosono, J. Am. Chem. Soc. **128**, 10012 (2006).

[32] A. Schilling, M. Cantoni, J. D. Guo, and H. R. Ott, Nature **363**, 56 (1993).

[33] A. P. Drozdov, M. I. Eremets, I. A. Troyan, V. Ksenofontov, and S. I. Shylin, Nature **525**, 73 (2015).

[34] P. J. Ray, Master's Thesis: Structural Investigation of La(2-x)Sr(x)CuO(4+y) - Following Staging as a Function of Temperature, University of Copenhagen, 2016.

[35] H. Fröhlich, Phys. Rev. **79**, 845 (1950).

[36] L. N. Cooper, Phys. Rev. **104**, 1189 (1956).

[37] M. Tinkham, *Introduction to Superconductivity: Second Edition.* (Dover publication, Mineola, NY, 2004).

[38] N. N. Bogoljubov, Il Nuovo Cimento 1955-1965 **7**, 794 (1958).

[39] J. G. Valatin, Il Nuovo Cimento 1955-1965 **7**, 843 (1958).

[40] K. S. Bedell, D. Coffey, D. E. Meltzer, D. Pines, and J. R. Schrieffer, *High Temperature Superconductivity* (Addison-Wesley, New York, 1990).

[41] M. Naito and K. Ueda, Supercond. Sci. Technol. **17**, R1 (2004).

[42] M. Rotter, M. Tegel, and D. Johrendt, Phys. Rev. Lett. **101**, 107006 (2008).

[43] X. C. Wang, Q. Q. Liu, Y. X. Lv, W. B. Gao, L. X. Yang, R. C. Yu, F. Y. Li, and C. Q. Jin, Solid State Commun. **148**, 538 (2008).

[44] D. N. Basov and A. V. Chubukov, Nat. Phys. (2011).

[45] P. J. Hirschfeld, M. M. Korshunov, and I. I. Mazin, Rep. Prog. Phys. **74**, 124508 (2011).

[46] N. D. Mermin and H. Wagner, Phys. Rev. Lett. **17**, 1133 (1966).

[47] T. Zhang, P. Cheng, W.-J. Li, Y.-J. Sun, G. Wang, X.-G. Zhu, K. He, L. Wang, X. Ma, X. Chen, Y. Wang, Y. Liu, H.-Q. Lin, J.-F. Jia, and Q.-K. Xue, Nat. Phys. **6**, 104 (2010).

[48] N. Reyren, S. Thiel, A. D. Caviglia, L. F. Kourkoutis, G. Hammerl, C. Richter, C. W. Schneider, T. Kopp, A.-S. Rüetschi, D. Jaccard, M. Gabay, D. A. Muller, J.-M. Triscone, and J. Mannhart, Science **317**, 1196 (2007).

[49] D. Dijkkamp, T. Venkatesan, X. D. Wu, S. A. Shaheen, N. Jisrawi, Y. H. Min-Lee, W. L. McLean, and M. Croft, Appl. Phys. Lett. **51**, 619 (1987).

[50] I. Bozovic, G. Logvenov, I. Belca, B. Narimbetov, and I. Sveklo, Phys. Rev. Lett. **89**, 107001 (2002).

[51] A. Inam, M. S. Hegde, X. D. Wu, T. Venkatesan, P. England, P. F. Miceli, E. W. Chase, C. C. Chang, J. M. Tarascon, and J. B. Wachtman, Appl. Phys. Lett. **53**, 908 (1988).

[52] C.-L. Song, Y.-L. Wang, Y.-P. Jiang, Z. Li, L. Wang, K. He, X. Chen, X.-C. Ma, and Q.-K. Xue, Phys. Rev. B **84**, 020503 (2011).

[53] W. Li, H. Ding, P. Deng, K. Chang, C. Song, K. He, L. Wang, X. Ma, J.-P. Hu, X. Chen, and Q.-K. Xue, Nat. Phys. **8**, 126 (2012).

[54] L. Vegard, Z. Phys. **5**, 17 (1921).

[55] E. Bauer, Z. Krist. **110**, 372 (1958).

[56] J. H. Neave, P. J. Dobson, B. A. Joyce, and J. Zhang, Appl. Phys. Lett. **47**, 100 (1985).

[57] C. Ratsch and J. A. Venables, J. Vac. Sci. Technol. A **21**, S96 (2003).

[58] J. A. Venables, Philos. Mag. J. Theor. Exp. Appl. Phys. **27**, 697 (1973).

[59] J. Shen, Z. Gai, and J. Kirschner, Surf. Sci. Rep. **52**, 163 (2004).

[60] J. A. Thornton, Annu. Rev. Mater. Sci. **7**, 239 (1977).

[61] A. Y. Cho and J. R. Arthur, Prog. Solid State Chem. **10**, 157 (1975).

[62] J. E. Davey and T. Pankey, J. Appl. Phys. **39**, 1941 (1968).

[63] J. J. Harris, B. A. Joyce, and P. J. Dobson, Surf. Sci. **103**, L90 (1981).

[64] T. H. Maiman, Nature **187**, 493 (1960).

[65] H. M. Smith and A. F. Turner, Appl. Opt. **4**, 147 (1965).

[66] N. Cherief, D. Givord, O. McGrath, Y. Otani, and F. Robaut, J. Magn. Magn. Mater. **126**, 225 (1993).

[67] R. W. Dreyfus, J. Appl. Phys. **69**, 1721 (1991).

[68] M.-C. Desjonqueres and D. Spanjaard, *Concepts in Surface Physics* (Spinger-Verlag, Heidelberg, 1993).

[69] P. P. Ewald, Acta Crystallogr. A **25**, 103 (1969).

[70] B. Gruzza and E. Gillet, Thin Solid Films **68**, 345 (1980).

[71] G. Binnig, H. Rohrer, C. Gerber, and E. Weibel, Phys. Rev. Lett. **49**, 57 (1982).

[72] J. Bardeen, Phys. Rev. Lett. **6**, 57 (1961).

[73] J. Tersoff and D. R. Hamann, Phys. Rev. Lett. **50**, 1998 (1983).

[74] J. Tersoff and D. R. Hamann, Phys. Rev. B **31**, 805 (1985).

[75] I. Giaever, Phys. Rev. Lett. **5**, 147 (1960).

[76] J.-F. Jia, X. Ma, X. Chen, T. Sakurai, and Q.-K. Xue, J. Phys. Appl. Phys. **44**, 464007 (2011).

[77] T. Hänke, S. Sykora, R. Schlegel, D. Baumann, L. Harnagea, S. Wurmehl, M. Daghofer, B. Büchner, J. van den Brink, and C. Hess, Phys. Rev. Lett. **108**, 127001 (2012).

[78] S. Chi, S. Grothe, R. Liang, P. Dosanjh, W. N. Hardy, S. A. Burke, D. A. Bonn, and Y. Pennec, Phys. Rev. Lett. **109**, 087002 (2012).

[79] M. P. Allan, A. W. Rost, A. P. Mackenzie, Y. Xie, J. C. Davis, K. Kihou, C. H. Lee, A. Iyo, H. Eisaki, and T.-M. Chuang, Science **336**, 563 (2012).

[80] S. Grothe, S. Chi, P. Dosanjh, R. Liang, W. N. Hardy, S. A. Burke, D. A. Bonn, and Y. Pennec, Phys. Rev. B **86**, 174503 (2012).

[81] T. Hanaguri, K. Kitagawa, K. Matsubayashi, Y. Mazaki, Y. Uwatoko, and H. Takagi, Phys. Rev. B **85**, 214505 (2012).

[82] T. Hanaguri, S. Niitaka, K. Kuroki, and H. Takagi, Science **328**, 474 (2010).

[83] A. Kreisel, R. Nelson, T. Berlijn, W. Ku, R. Aluru, S. Chi, H. Zhou, U. R. Singh, P. Wahl, R. Liang, W. N. Hardy, D. A. Bonn, P. J. Hirschfeld, and B. M. Andersen, Phys. Rev. B **94**, (2016).

[84] V. B. Nascimento, A. Li, D. R. Jayasundara, Y. Xuan, J. O'Neal, S. Pan, T. Y. Chien, B. Hu, X. B. He, G. Li, A. S. Sefat, M. A. McGuire, B. C. Sales, D. Mandrus, M. H. Pan, J. Zhang, R. Jin, and E. W. Plummer, Phys. Rev. Lett. **103**, 076104 (2009).

[85] F. Massee, S. de Jong, Y. Huang, J. Kaas, E. van Heumen, J. B. Goedkoop, and M. S. Golden, Phys. Rev. B **80**, 140507 (2009).

[86] Y. Yin, M. Zech, T. L. Williams, X. F. Wang, G. Wu, X. H. Chen, and J. E. Hoffman, Phys. Rev. Lett. **102**, 097002 (2009).

[87] H. Zhang, J. Dai, Y. Zhang, D. Qu, H. Ji, G. Wu, X. F. Wang, X. H. Chen, B. Wang, C. Zeng, J. Yang, and J. G. Hou, Phys. Rev. B **81**, 104520 (2010).

[88] G. Li, X. He, J. Zhang, R. Jin, A. S. Sefat, M. A. McGuire, D. G. Mandrus, B. C. Sales, and E. W. Plummer, Phys. Rev. B **86**, 060512 (2012).

[89] J. E. Hoffman, K. McElroy, D.-H. Lee, K. M. Lang, H. Eisaki, S. Uchida, and J. C. Davis, Science **297**, 1148 (2002).

[90] B. Stöger, M. Hieckel, F. Mittendorfer, Z. Wang, M. Schmid, G. S. Parkinson, D. Fobes, J. Peng, J. E. Ortmann, A. Limbeck, Z. Mao, J. Redinger, and U. Diebold, Phys. Rev. B **90**, 165438 (2014).

[91] G. J. H. M. Rijnders, G. Koster, D. H. A. Blank, and H. Rogalla, Appl. Phys. Lett. **70**, 1888 (1997).

[92] M. T. Yurtcan, O. Simsek, M. Yilmaz, U. C. Hasar, M. Ertugrul, and O. S. Bayram, J. Supercond. Nov. Magn. **26**, 1873 (2013).

[93] M. T. Yurtcan, Ö. Şimşek, Ö. Bayram, and M. Ertuğrul, East. Anatol. J. Sci. **3**, 1 (n.d.).

[94] S. S. Bhagwat, A. R. Bhangale, J. M. Patil, and V. S. Shirodkar, Braz. J. Phys. **30**, 541 (2000).

[95] M. Z. Cieplak, M. Berkowski, S. Guha, E. Cheng, A. S. Vagelos, D. J. Rabinowitz, B. Wu, I. E. Trofimov, and P. Lindenfeld, Appl. Phys. Lett. **65**, 3383 (1994).

[96] G. Ilonca, A. V. Pop, T. Jurcut, C. Lung, G. Stiufiuc, R. Stiufiuc, O. Furdui, E. Mococeanu, and R. Deltour, Mod. Phys. Lett. B **14**, 639 (2000).

[97] F. V. E. Hensling, C. Xu, F. Gunkel, and R. Dittmann, Sci. Rep. **7**, 39953 (2017).

[98] L. Iglesias, A. Sarantopoulos, C. Magén, and F. Rivadulla, Phys. Rev. B **95**, 165138 (2017).

[99] S. Yamamoto, T. Sumita, Sugiharuto, A. Miyashita, and H. Naramoto, Thin Solid Films **401**, 88 (2001).

[100] G. Rijnders, The Initial Growth of Complex Oxides: Study and Manipulation, University of Twente, 2001.

[101] S. H. Pan, International Patent Publication Number WO 93/19494 (1993).

[102] J. E. Hoffman, Rep. Prog. Phys. **74**, 124513 (2011).

[103] M. Rotter, M. Tegel, D. Johrendt, I. Schellenberg, W. Hermes, and R. Pöttgen, Phys. Rev. B **78**, 020503 (2008).

[104] K. Iida, J. Haenisch, R. Huehne, F. Kurth, M. Kidszun, S. Haindl, J. Werner, L. Schultz, and B. Holzapfel, Appl. Phys. Lett. **95**, 192501 (2009).

[105] T. Katase, Y. Ishimaru, A. Tsukamoto, H. Hiramatsu, T. Kamiya, K. Tanabe, and H. Hosono, Appl. Phys. Lett. **96**, 142507 (2010).

[106] C. Tarantini, S. Lee, Y. Zhang, J. Jiang, C. W. Bark, J. D. Weiss, A. Polyanskii, C. T. Nelson, H. W. Jang, C. M. Folkman, S. H. Baek, X. Q. Pan,

A. Gurevich, E. E. Hellstrom, C. B. Eom, and D. C. Larbalestier, Appl. Phys. Lett. **96**, 142510 (2010).

[107] K. Iida, S. Haindl, T. Thersleff, J. Hänisch, F. Kurth, M. Kidszun, R. Hühne, I. Mönch, L. Schultz, B. Holzapfel, and R. Heller, Appl. Phys. Lett. **97**, 172507 (2010).

[108] K. Iida, J. Hänisch, S. Trommler, V. Matias, S. Haindl, F. Kurth, I. L. del Pozo, R. Hühne, M. Kidszun, J. Engelmann, L. Schultz, and B. Holzapfel, Appl. Phys. Express **4**, 013103 (2010).

[109] M. Kawasaki, K. Takahashi, T. Maeda, R. Tsuchiya, M. Shinohara, O. Ishiyama, T. Yonezawa, M. Yoshimoto, and H. Koinuma, Science **266**, 1540 (1994).

[110] H.-J. Shin, S. H. Kim, H. J. Yang, and Y. Kuk, Nanotechnology **18**, 175304 (2007).

[111] T. Katase, H. Hiramatsu, T. Kamiya, and H. Hosono, Appl. Phys. Express **3**, 063101 (2010).

[112] J. H. Tapp, Z. Tang, B. Lv, K. Sasmal, B. Lorenz, P. C. W. Chu, and A. M. Guloy, Phys. Rev. B **78**, 060505 (2008).

[113] H. Kim, M. A. Tanatar, Y. J. Song, Y. S. Kwon, and R. Prozorov, Phys. Rev. B **83**, 100502 (2011).

[114] K. Umezawa, Y. Li, H. Miao, K. Nakayama, Z.-H. Liu, P. Richard, T. Sato, J. B. He, D.-M. Wang, G. F. Chen, H. Ding, T. Takahashi, and S.-C. Wang, Phys. Rev. Lett. **108**, 037002 (2012).

[115] S. J. Zhang, X. C. Wang, R. Sammynaiken, J. S. Tse, L. X. Yang, Z. Li, Q. Q. Liu, S. Desgreniers, Y. Yao, H. Z. Liu, and C. Q. Jin, Phys. Rev. B **80**, 014506 (2009).

[116] M. Gooch, B. Lv, J. H. Tapp, Z. Tang, B. Lorenz, A. M. Guloy, and P. C. W. Chu, EPL Europhys. Lett. **85**, 27005 (2009).

[117] D. J. Singh, Phys. Rev. B **78**, 094511 (2008).

[118] I. I. Mazin, D. J. Singh, M. D. Johannes, and M. H. Du, Phys. Rev. Lett. **101**, 057003 (2008).

[119] S. V. Borisenko, V. B. Zabolotnyy, D. V. Evtushinsky, T. K. Kim, I. V. Morozov, A. N. Yaresko, A. A. Kordyuk, G. Behr, A. Vasiliev, R. Follath, and B. Büchner, Phys. Rev. Lett. **105**, 067002 (2010).

[120] A. Lankau, K. Koepernik, S. Borisenko, V. Zabolotnyy, B. Büchner, J. van den Brink, and H. Eschrig, Phys. Rev. B **82**, 184518 (2010).

[121] K. Chang, P. Deng, T. Zhang, H.-C. Lin, K. Zhao, S.-H. Ji, L.-L. Wang, K. He, X.-C. Ma, X. Chen, and Q.-K. Xue, EPL Europhys. Lett. **109**, 28003 (2015).

[122] M. J. Pitcher, D. R. Parker, P. Adamson, S. J. C. Herkelrath, A. T. Boothroyd, R. M. Ibberson, M. Brunelli, and S. J. Clarke, Chem. Commun. **0**, 5918 (2008).

국 문 초 록

주사형 터널링 현미경을 이용한 에피탁시 성장된 고온 초전도체 박막의 표면 연구

이선욱

물리천문학부

서울대학교 대학원

임계 온도 이하에서 직류 저항이 없으며, 자기장을 밀어내는 독특한 현상으로 대표되는 초전도현상은 그 발견 이래 응집물질물리 분야에서 가장 활발히 연구되는 분야이다. 많은 초전도의 비밀이 BCS 이론의 미시적인 접근으로 풀리게 되었지만, 최근 발견된 구리산화물 및 철기반 초전도체와 같은 고온 초전도체는 새로운 초전도 기전의 설명을 필요로 한다. 이 연구에서는 고온 초전도체 이해를 넓히기 위해, 저온 주사형 터널링 현미경을 통해서 에피탁시 성장된 고온 초전도체 박막의 연구를 실시하였다. 박막의 에피탁시 성장을 위해서 이 연구에서는 분자선 에피탁시 기법과 펄스 레이저 증착법을 이용하여 박막을 성장할 수 있는 장비를 제작하였고, 그 구성 및 디자인의 고려사항들을 수록하였다. 그리고 성장한 박막의 측정을 진공 내부에서 실시할 수 있도록

주사형 터널링 현미경과 레이저 분자선 에피탁시 장비를 결합하여 여러 종류의 초전도체 박막을 성장시키고 측정할 수 있었다.

펄스 레이저 증착 기법을 이용한 코발트 도핑된 바륨-철-비소 고온 초전도 화합물 박막에서는 $2\sqrt{2} \times 2\sqrt{2}$ R45° 표면 재구성이 나타났으며, 바륨 레이어에 의한 초전도 갭의 가림 효과를 확인하였다. 그리고 초전도 갭 근처에서 전하 밀도 파동을 관찰하였다. 또 다른 철 기반 고온 초전도체인 리튬-철-비소 화합물 박막은 최초로 펄스 레이저 증착 기법을 이용해서 성장시켰다. 성장 조건 및 성장의 최적화는 주사형 터널링 현미경과 반사 고에너지 전자선 회절법을 통해서 실시되었다. 그리고 성장 중단 기법을 통해서 박막의 품질을 향상시키고, 적층 구조적 성장에 더 가깝게 하였다.

주요어 : 초전도체, 철기반 초전도체, 박막 초전도체, 펄스 레이저 증착, 주사형 탐침 현미경

학 번 : 2011-23276